Multiple-omics analysis reveals a dedifferentiation-immune loop in intrahepatic cholangiocarcinoma

Jian Ruan,[1,14] Qiong Li,[1,14] Yuzhi Jin,[1,14] Jie Yin,[12,13,14] Chanqi Ye,[1,14] Fei Cheng,[2,14] Shuaishuai Xu,[1] Ruyin Chen,[1] Chuan Liu,[1] Xiaoxiang Rong,[3] Ming Jiang,[4] Wenguang Fu,[5] Dayong Zheng,[6] Jinzhang Chen,[7] Xuanwen Bao,[1] Houhong Wang,[8,9] Jianpeng Sheng,[10,11] and Peng Zhao[1]

[1]Department of Medical Oncology, The First Affiliated Hospital, School of Medicine, Zhejiang University and Key Laboratory of Cancer Prevention and Intervention, Ministry of Education, Hangzhou 310003, Zhejiang Province, People's Republic of China; [2]Pathology Department, The First Affiliated Hospital, School of Medicine, Zhejiang University, Hangzhou 310003, Zhejiang Province, People's Republic of China; [3]Department of Oncology, Nanfang Hospital, Southern medical University, Guangzhou 510000, Guangdong Province, People's Republic of China; [4]The Children's Hospital, Zhejiang University School of Medicine and National Clinical Research Center for Child Health, Hangzhou 310058, Zhejiang Province, People's Republic of China; [5]Department of Hepatobiliary Surgery, The Affiliated Hospital of Southwest Medical University, Luzhou 646000, Sichuan Province, People's Republic of China; [6]Cancer Center, Integrated Hospital of Traditional Chinese Medicine, Southern Medical University, Guangzhou 510315, Guangdong Province, People's Republic of China; [7]Department of Oncology, Nanfang Hospital, Southern medical University, Guangzhou 510000, Guangdong Province, People's Republic of China; [8]Department of General Surgery, The First Hospital Affiliated to Fuyang Normal University, Fuyang 236006, Anhui Province, People's Republic of China; [9]Department of General Surgery, The Affiliated Bozhou Hospital of Anhui Medical University, Bozhou 236800, Anhui Province, People's Republic of China; [10]College of Computer Science and Technology, Nanjing University of Aeronautics and Astronautics, Nanjing 211106, Jiangsu Province, People's Republic of China; [11]Chinese Institutes for Medical Research, Beijing 100000, People's Republic of China; [12]Center for Genetic Medicine, the Fourth Affiliated Hospital, Zhejiang University School of Medicine, Hangzhou, Zhejiang, China; [13]Institute of Genetics, Zhejiang University and Department of Genetics, Zhejiang University School of Medicine, Hangzhou, Zhejiang, China

Intrahepatic cholangiocarcinoma (ICC) is known for its diverse cell types and resistance to standard treatments, highlighting the importance of understanding its tumor microenvironment (TME) for improved prognostic accuracy and therapeutic innovation. Our study used a multi-omics approach to analyze the ICC TME in both human and mouse samples, linking survival outcomes to the complex cellular interactions within the TME. We discovered a dedifferentiation phenomenon in ICC cells driven by the Yes-associated protein (YAP) pathway, influenced by tumor-associated macrophages (TAMs). Conversely, ICC cells promoted an immunosuppressive environment in TAMs. Targeting TAMs in a transgenic mouse model disrupted this loop, enhancing T cell responses and suggesting a novel immunotherapy avenue for ICC. Our findings reveal a reciprocal dedifferentiation-immunosuppression loop between ICC cells and TAMs, advocating TAM targeting as a promising therapy and highlighting the potential of macrophage modulation in ICC treatment.

INTRODUCTION

Intrahepatic cholangiocarcinoma (ICC), which accounts for 15% of primary liver cancers, has experienced an increase in both incidence and mortality in recent decades.[1–3] ICC is often diagnosed at an advanced stage due to its complicated clinical features and lack of typical symptoms and diagnostic biomarkers, which are also associated with a high recurrence rate. Despite enormous breakthroughs in the treatment of malignancies, little progress toward improving the prognosis of ICC patients has been achieved.[4] Owing to the desmoplastic tumor microenvironment (TME) of

ICC, cytotoxic chemotherapy increases survival by less than 1 year.[5,6] The lack of typical biomarkers has restrained the application of molecular targeted therapy, and surgical resection or liver transplantation remain the prime regimens for early-stage ICC patients.[7]

The ICC TME is highly heterogeneous and consists of cancer, stromal, and various immune cells, forming a complicated and dynamic ecosystem. The heterogeneity of the ICC TME distinguishes the responses and prognoses of ICC patients. A TME-based sub-classification divided ICC patients into four groups: immune desert, immunogenic, myeloid, and mesenchymal. Among these groups, the myeloid subtype features infiltration of M2-polarized tumor-associated macrophages (TAMs) and a survival disadvantage,[8] supporting the

Correspondence: Houhong Wang, Department of General Surgery, The First Hospital Affiliated to Fuyang Normal University, Fuyang 236006, Anhui Province, People's Republic of China.
**E-mail:** whh6366@163.com
Correspondence: Jianpeng Sheng, College of Computer Science and Technology, Nanjing University of Aeronautics and Astronautics, Nanjing 211106, Jiangsu Province, People's Republic of China.
E-mail: shengjp@zju.edu.cn
Correspondence: Peng Zhao, Department of Medical Oncology, The First Affiliated Hospital, School of Medicine, Zhejiang University and Key Laboratory of Cancer Prevention and Intervention, Ministry of Education, Hangzhou 310003, Zhejiang Province, People's Republic of China.
E-mail: zhaop@zju.edu.cn
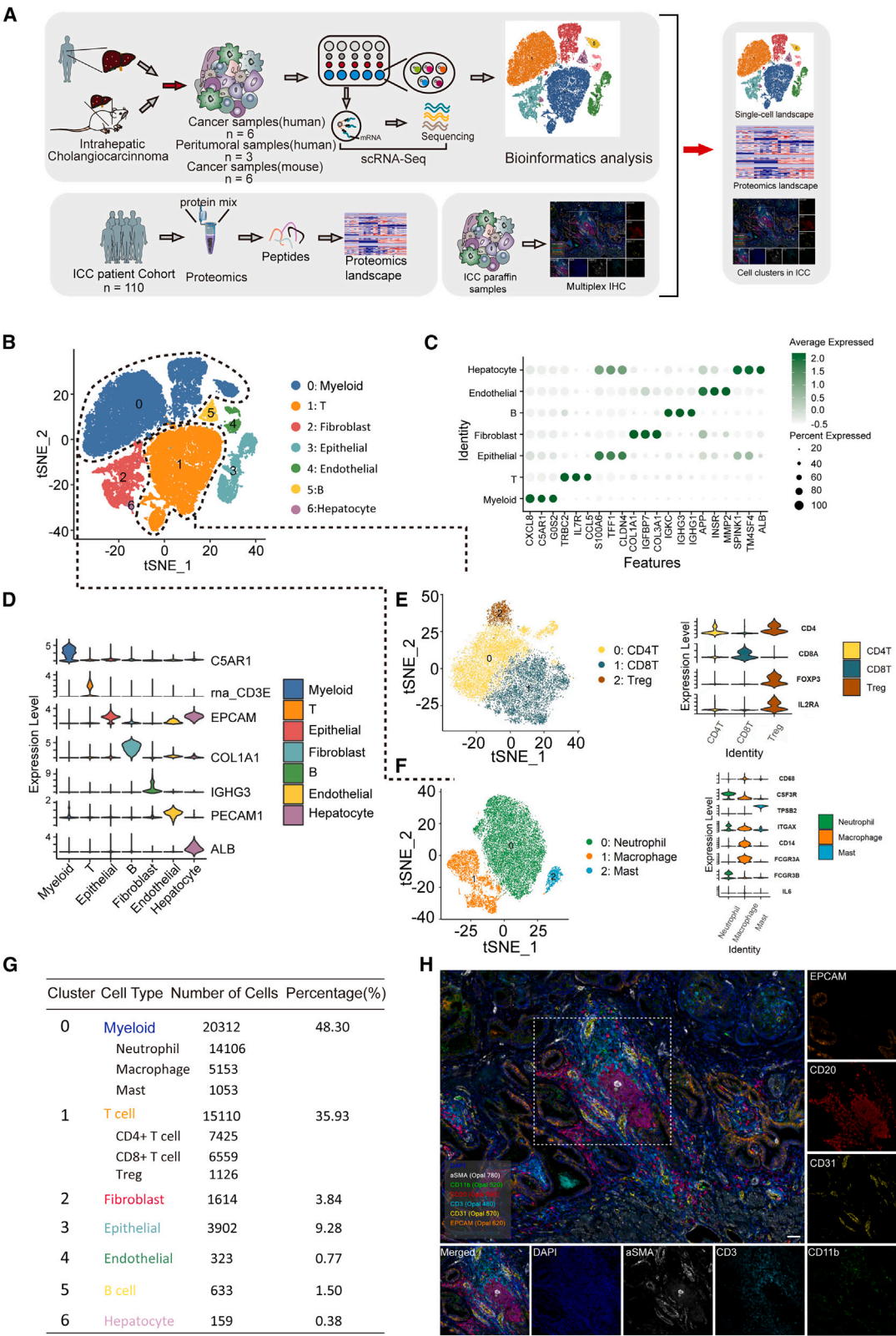
leading role of macrophages in the TME for ICC development. TAMs in the ICC TME can be polarized into M1 cells with antitumor activities and M2 cells with tumor-promoting functions. TAMs polarized to the M2 phenotype secrete molecules, including interleukin (IL)-6, IL-1, transforming growth factor (TGF)-β, vascular endothelial growth factor (VEGF), and platelet-derived growth factor (PDGF), to accelerate ICC development. An increasing number of M2 cells is a negative indicator of ICC prognosis.[9] However, the detailed mechanism by which TAM affects the ICC TME is still unclear.

Several recent reports have shown that increased malignant cell stemness regulated by various pathways is associated with patient's prognosis.[10,11] For example, hypoxia has been shown to induce Sonic Hedgehog signaling, regulating cancer cell stemness.[12] Loss of ARID1A was found to promote tumor cell stemness based on ALDH1A1 expression.[13] Yes-associated protein (YAP) was also shown to maintain putative cancer cell stemness through dedifferentiation.[14,15] However, the mechanism by which immune cells, especially macrophages, affect the dedifferentiation of ICC tumor cells remains unknown.

Advances in immunotherapy have shown robust activity in malignancies such as non-small cell lung cancer, melanoma, and lymphoma. There are currently a few promising results in clinical trials of ICC treatments, including KEYNOTE-028, which reported the interim safety and efficacy of the anti-programmed cell death protein 1 (PD-1) antibody pembrolizumab for patients with programmed cell death ligand 1 (PD-L1)-positive biliary tract cancer, encouraging exploration of the rationale and effectiveness of immunotherapy in ICC.[7]

Here, we depicted the landscape of the ICC TME using single-cell RNA sequencing (scRNA-seq), proteomic analysis, and multiplex immunohistochemistry (mIHC). We found that the malignant tumor cells underwent both dedifferentiation and proliferation. In addition, these two processes were decoupled from each other, both of which were assisted by TAM. Furthermore, we showed that the disruption of the dedifferentiation-immunosuppression loop in TAM-targeting transgenic mice recruited more T cells into ICC tissues and reduced the number of tumor lesions, which sheds light on future macrophage-based immunotherapy.

RESULTS

The multi-omics landscape of ICC tumoral tissues

To explore the cellular diversity and molecular signature of ICC, we performed multi-omics profiling of the ICC TME (Figure 1A). scRNA-seq profiling of six ICC samples and three corresponding peritumoral tissues was performed using BD Rhapsody sequencing to better capture myeloid cells (Figure 1A). In addition, we collected a set of 110 ICC tumor specimens with clinical information and performed proteomic analysis (Figure 1A). Furthermore, the key bioprocesses identified via scRNA-seq and proteomic analysis were validated by immunohistochemistry (IHC) and IHC staining of the clinical sample set (Figure 1A). We also established a mouse ICC model and performed scRNA-seq to confirm the key findings revealed by the multi-omics analysis of human ICC samples (Figure 1A).

In terms of scRNA-seq analysis, after initial quality control, we acquired single-cell transcriptomes for a total of 46,502 cells from six ICC tumor sites and three corresponding peritumoral sites. To dissect the cellular composition of the tumors, we applied t-distributed stochastic neighbor embedding (t-SNE) and a graph-based algorithm for dimensionality reduction and cell cluster determination. These cells were assigned to seven main cellular clusters (Figure 1B).

In order to ascertain the identity of individual cell clusters, cluster-specific marker genes were generated by performing differential gene expression analysis (Figure 1C; Table S4). SingleR[16] with manual aid identified cell clusters utilizing cell type signatures. For example, epithelial cell markers such as epithelial cell adhesion molecule (EPCAM) were used to define epithelial cells (Figure 1D). COL1A1 was used to define fibroblasts (Figure 1D)[17] and PECAM1 was used to define endothelial cells (Figure 1D).[18] ALB was used to define hepatocytes (Figure 1D).[19]

Notably, our scRNA-seq data revealed various subsets of immune cells. CD3+ T cells can be divided into CD4+ and CD8+ T cells. Regulatory T cells (Tregs) could be clearly distinguished from other CD4+ T cells by FOXP3 and IL2RA expression (Figure 1E). In addition, myeloid cells showed high levels of C5AR1[20] (Figure 1D), including CD68+ macrophages, CSF3R+ neutrophils,[21,22] and TPSB2+ mast cells[23] (Figure 1F). ITGAX was found to be expressed in macrophages and neutrophils[24] (Figure 1F). We further identified CD14 and

---

Figure 1. The multi-omics atlas in ICC tumoral tissues

(A) Schematic of multi-omics analysis workflow. Six human ICC samples, three human ICC peritumoral samples, and six mouse ICC samples were digested into single cells and sequenced using the BD Rhapsody platform to perform scRNA-seq analysis. Proteomic analysis was performed with 110 ICC tumor specimens. IHC and mIHC stainings of the clinical sample set were used to validate the key bioprocess of multi-omics analysis. (B) t-SNE plot was used to identify the primary cell types in ICC based on the scRNA-seq data. (C) A heatmap was used to illustrate the expression levels of specific markers in each cell population. The color key ranging from white to green indicates relative expression levels, with white representing low expression and green representing high expression. (D) Violin plots displayed the expression levels of specific markers for each cell type in ICC. (E) The t-SNE plot identified the main cell types of T cells, displayed on the left side. Additionally, the violin plots on the right side showcased the expression levels of specific markers for each T cell type. (F) The t-SNE plot in identified the main cell types of myeloid cells on the left side. The expression levels of specific markers for each myeloid cell type were shown in the violin plots on the right side. (G) The information on the cell number and percentage of assigned cell types. (H) mIHC was performed to validate the major cellular components of the ICC TME. The scale bar in the image represents 50 μm.
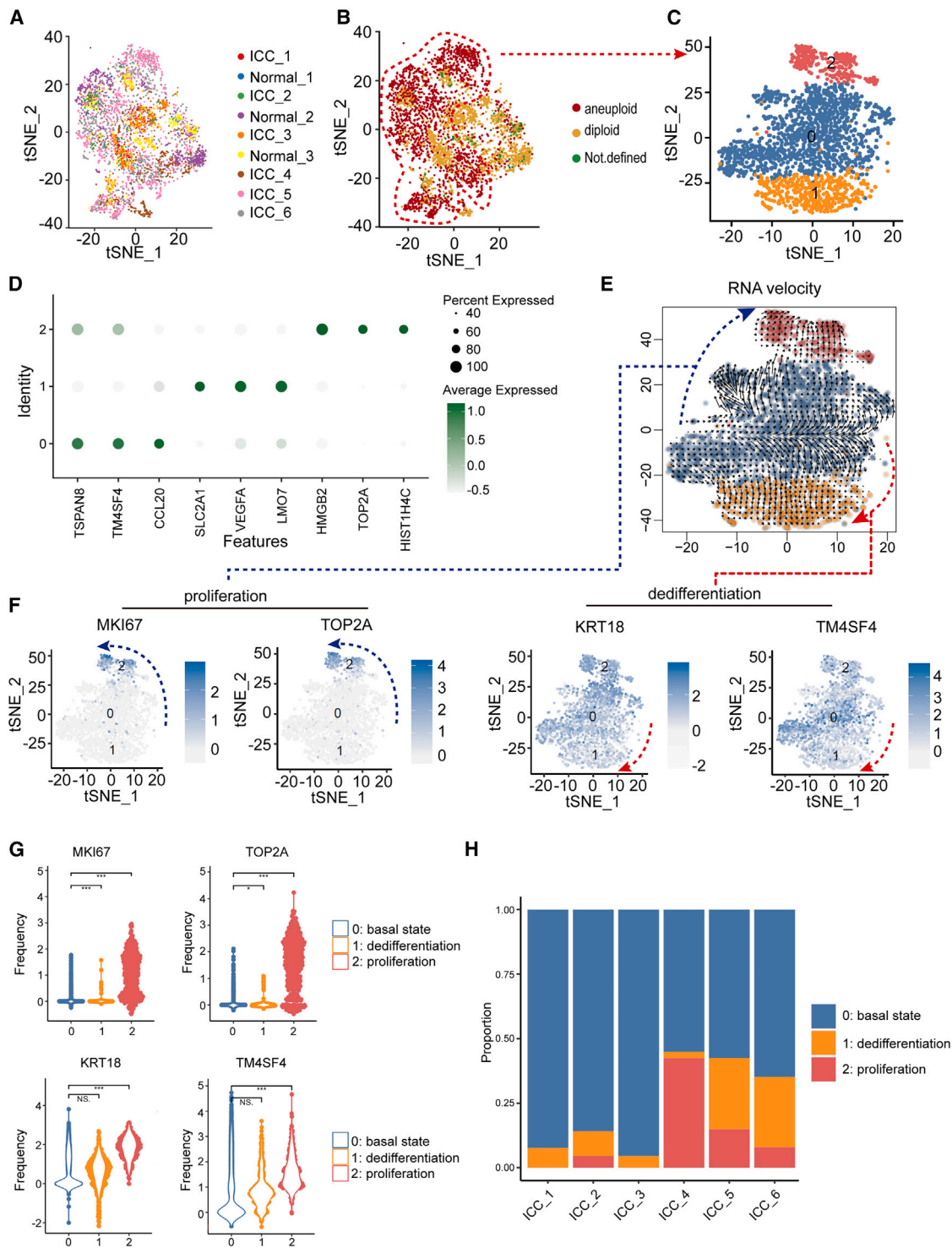
Figure 2. Decoupled dedifferentiation and proliferation processes of malignant cells in ICC tissues

(A and B) The t-SNE plot was used to identify aneuploid cells and diploid cells in the total epithelial cell population. This analysis was based on the scRNA-seq data obtained from six tumoral tissues and three peritumoral tissues. (C) The t-SNE plot revealed the presence of three distinct subgroups within the malignant cells, which were identified based on the expression levels of specific feature genes. (D) A heatmap was generated to visualize the expression levels of the feature genes within each subgroup of malignant cells. The color key ranging from gray to green represents the relative expression levels, with gray indicating low expression and green indicating high expression.

(legend continued on next page)

FCGR3A (CD16A) expression in macrophages and FCGR3B (CD16B) in neutrophils (Figure 1F), indicating that various myeloid cells might engage different pathogen-association molecule pattern receptors (CD14, CD16 A/B) for their specific immune responses in the ICC TME.

The detailed frequency of each cell population is shown (Figure 1G). The major cellular components and percentage of each cell population were identified via scRNA-seq and validated using mIHC (Figures 1H, S1A, and S1B), including α-SMA⁺ fibroblasts, CD11b⁺ myeloid cells, CD20⁺ B cells, CD3⁺ T cells, CD31⁺ endothelial cells, and EPCAM⁺ epithelial cells. We also performed mIHC staining to distinguish hepatocytes from epithelial cells (Figure S1C). In the proteomic analysis, 110 ICC tumor specimens and the internal reference control were processed in 10 batches, and a low batch variance was observed (Figure S2A). We identified 10,888 proteins (Figure S2B), and their distribution within the cell is shown (Figure S2C).

Altogether, our multi-omics landscape covered the major cellular and proteomic components of the ICC TME.

Decoupled dedifferentiation and proliferation processes of malignant cells

Next, we defined the heterogeneity within malignant cells by performing refined clustering of malignant cells. Before further cell clustering, *bona fide* malignant cells were first identified through copyKAT and inferCNV analysis,[25,26] which could differentiate aneuploid and diploid cells based on gene copy variations. We found that most epithelial cells were aneuploid malignant cells (Figures 2A, 2B, and S3A).

Next, we performed t-SNE and cell clustering analyses on the aneuploid malignant cells. Based on the results of copyKAT and inferCNV analysis above, the malignant cell population was further divided into three subgroups and four subgroups, respectively (Figures 2C and S3B), and feature genes were selected for each subgroup (Figures 2D and S3C; Table S5).

To identify the developmental trajectory within malignant cells, we performed RNA velocity analysis of malignant cells.[27] We found that the malignant cells underwent two different developmental routes (Figure 2E). We noticed that the malignant cell markers (KRT18 and TM4SF4)[28,29] were downregulated from malignant subclusters 0 to 1. The proliferative cell markers (MKI67 and TOP2A) were upregulated in malignant subclusters 0 to 2 (Figure 2F). The above results indicated that the dedifferentiation and proliferation processes were decoupled

within the malignant cell population (Figures 2E and 2F). Consistent with the findings of the copyKAT analysis, the results obtained from the inferCNV analysis identified the same two developmental trajectories within malignant cells (Figures S3D and S3E). The frequencies of the malignant cell markers (KRT18 and TM4SF4) and proliferative cell markers (MKI67 and TOP2A) were consistent with our t-SNE analysis results (Figure 2G). In addition, we checked the distribution of each malignant cell subset and ruled out the possibility that the dedifferentiation or proliferation subset was derived from specific patients. The distribution pattern of malignant cell subsets indicated that ICC malignant cells were a mixture of the basal state (cluster 0), dedifferentiation state (cluster 1), and proliferation state (cluster 2). The compositions of the three states varied among different ICC patients (Figure 2H). It is worth noting that dedifferentiation and proliferation processes were not observed in epithelial cells from peritumoral tissues (Figures S4A and S4B).

To confirm our findings of decoupled dedifferentiation and proliferation processes in ICC patients, we analyzed an independent dataset of 12 ICC tumoral samples from Ma et al.[30] (Figure S4C). Similarly, we identified six major cell populations: T cells, cancer-associated fibroblasts, TAM, tumor endothelial cells (TECs), B cells, and epithelial cells (Figure S4D). Within the 1,441 epithelial cells, most cells were aneuploid malignant cells (Figure S4E). Aneuploid malignant cells consisted of three clusters (Figure S4E). Consistent with our in-house datasets, we identified basal state malignant cells (cluster 0, KRT18⁺ TM4SF4⁺), proliferating malignant cells (cluster 1, Ki67⁺ TOP2A⁺), and dedifferentiated malignant cells (cluster 2, KRT18ˡᵒʷ, TM4SF4ˡᵒʷ) (Figure S3F). Pseudo-time analysis of the three clusters also indicated bifurcated developmental routes of dedifferentiated and proliferating cells (Figure S4G). Twelve ICC patients also showed mixtures of these three states (Figure S4H).

Taken together, our detailed examination of the relationship between the different subgroups of malignant cells allowed us to discover decoupled dedifferentiation and proliferation processes in ICC patients.

Dedifferentiation and proliferation states of ICC malignant cells reflect poor clinical outcomes

Next, we aimed to determine the relationship between patient prognosis and malignant cell dedifferentiation/proliferation. Two distinct gene sets based on malignant cell cluster 1 and 2 feature genes were built to represent the dedifferentiation and proliferation processes, respectively (Table S5). These two gene sets were used for genome enrichment analysis (GSEA) score calculation based on each sample of proteomic data from in-house 110 patients' proteomic data. The

(E) RNA velocity analysis was conducted to determine the developmental trajectory of the malignant cells. This analysis revealed the existence of two distinct developmental trajectories within the malignant cell population. (F) The t-SNE plots were utilized to examine the expression levels of proliferative cell markers (MKI67 and TOP2A) and malignant cell markers (KRT18 and TM4SF4) in the different malignant cell subgroups. The color key ranging from gray to blue represents the relative expression levels, with gray indicating low expression and blue indicating high expression. (G) The violin plots were utilized to examine the expression levels of proliferative cell markers (MKI67 and TOP2A) and malignant cell markers (KRT18 and TM4SF4) in the different malignant cell subgroups. (H) A 100% stacked bar chart was created to present the distribution of the four major malignant subgroups in the scRNA-seq datasets obtained from the six ICC samples. The chart provides information on the relative proportions of each subgroup within the tumor samples.
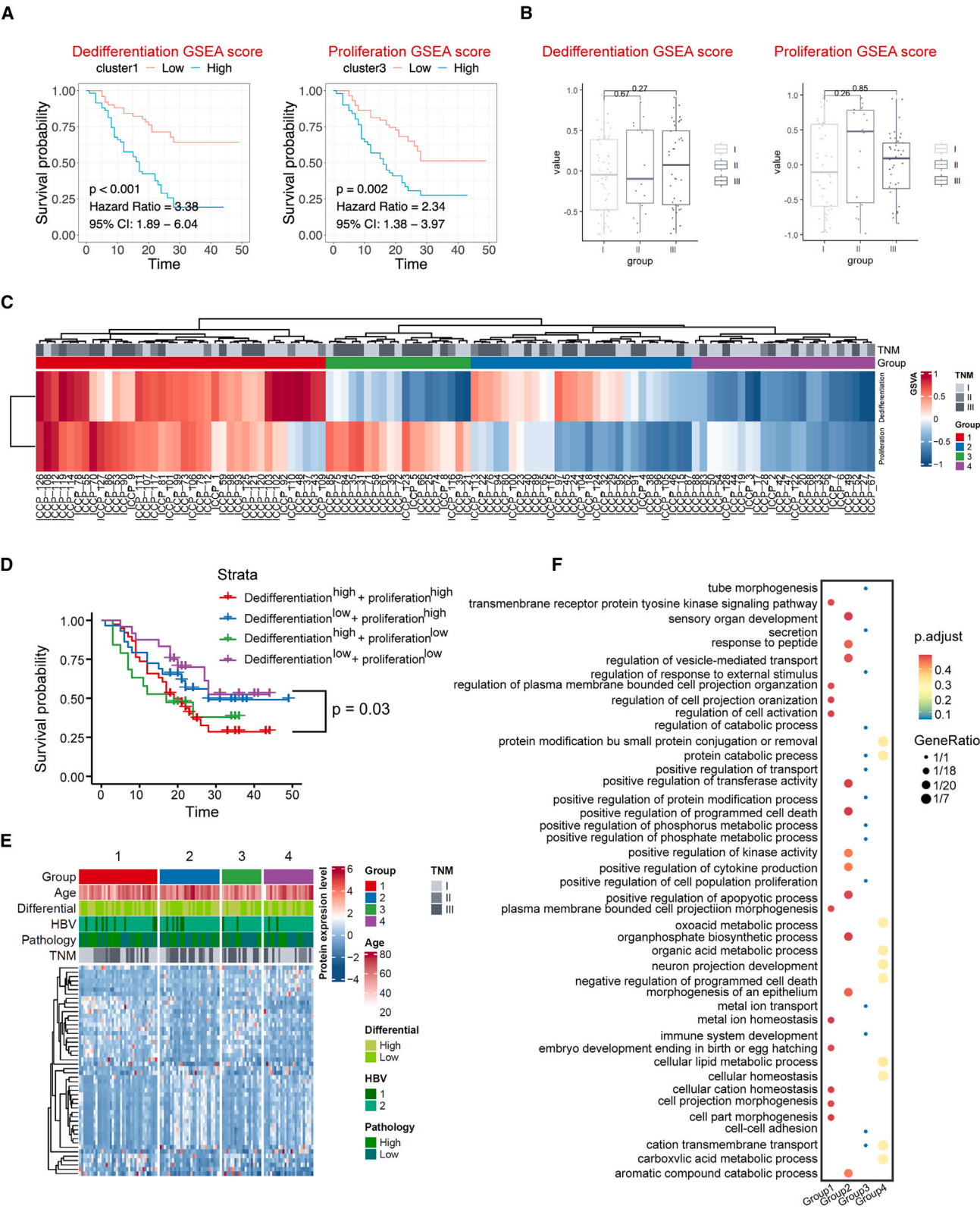
(legend on next page)

patient cohort was categorized into high or low classes (using the best cutoff method) based on their GSEA score calculated from proteomic data for the dedifferentiation and proliferation of malignant cell subclusters. The results showed that patients with dedifferentiation and proliferation of malignant cells had worse prognosis (Figure 3A). Our results showed that the tumor, node, metastasis (TNM) stage of ICC patients was not correlated with the enrichment of the dedifferentiation and proliferation status of malignant cells (Figure 3B).

In addition, we wanted to determine whether the state of malignant cells could facilitate the molecular grouping of ICC patients. The basal state, proliferation state, and dedifferentiation state were deconvoluted based on GSEA methods, using features of genes of malignant cluster 0 (basal state), cluster 1 (dedifferentiation), and cluster 2 (proliferation). Our in-house proteomics datasets from 110 ICC patients were separated into four major categories based on the malignant cell state (Figure 3C). Group 1 showed dedifferentiation[high] and proliferation[high] state signatures, while group 2 showed more significant dedifferentiation[high] and proliferation[low] state signatures (cluster 1 features). Group 3 showed more dedifferentiation[low] and proliferation[high] state signatures (cluster 2 features), whereas group 4 showed dedifferentiation[low] and proliferation[low] signatures (cluster 0 features) (Figure 3C). Among the four groups, the group with more dedifferentiation[high] and proliferation[high] state signatures showed the worst prognosis, and the group with dedifferentiation[low] and proliferation[low] signatures showed the best prognosis (Figure 3D). The protein features of each group are shown in Figure 3E. In addition, we performed Cox analysis to remove the confounding effects of sex and age (Figure S5). Furthermore, Gene Ontology (GO) analysis was performed for the feature proteins of each group, and we noticed distinct biological activities across different groups (Figure 3F). For example, group 4 (basal state enriched) showed increased epithelial cell differentiation. Group 3 (proliferation enriched) showed more positive regulation of cell movement, whereas group 2 (dedifferentiation enriched) showed more activity of lipid and ion transport (Figure 3F).

Overall, we found that the dedifferentiation and proliferation of malignant cells were associated with poor prognosis with the integration analysis of scRNA-seq, transcriptomic, and proteomic datasets.

## Macrophages promote malignant cell dedifferentiation and proliferation

Next, we aimed to understand the mechanisms of malignant cell dedifferentiation and proliferation. The Hippo signaling pathway controls the molecular switch of malignant cell dedifferentiation.[31] We performed gene set variation analysis (GSVA) based on the Hippo signaling gene sets for all malignant cell clusters and found that the Hippo signaling pathway was enriched in the dedifferentiation of malignant cell cluster 1 (Figure 4A). In addition, malignant cell cluster 1 showed the highest Hippo signaling score (Figures S6A and S6B). We also observed strong Hippo signaling in ICC patients, as indicated by mIHC staining of active YAP1 and YAP1 (Figures 4B and S6C).

Previous reports indicated that macrophages could promote malignant cell dedifferentiation in thyroid and colon cancer.[32,33] We also observed that YAP[+] dedifferentiated malignant cells were heavily surrounded by macrophages (Figure 4B). Thus, we investigated whether macrophages regulate the dedifferentiation process of malignant ICC cells. First, macrophage heterogeneity was dissected. We identified CD68^{+} CD11b^{low} C1QA/B^{+} resident macrophages (ResMf),[34] CD68^{+} CD11b^{+} infiltrating macrophages (InfMf),[35] SPP1^{+} macrophages (SPP1^{+} Mf),[36] and CD1c^{+} dendritic cells (DCs)[37] (Figures 4C–4E), and the feature genes of each subgroup are shown in Table S6. Recently, Guilliams et al. performed a detailed analysis of human and mouse liver macrophages and identified six macrophage and DC subsets, including Kupffer cells and classical DCs (Figures S7A and S7B). We compared ICC TAMs with liver macrophages and DCs from Guilliams et al. by using AUCell.[38] Both resident macrophages and SPP1^{+} macrophages seemed to be mixtures of Kupffer cells, indicating the mixed origins of TAM. The infiltrating macrophages in ICC were not similar to those in liver monocytes, DCs, or macrophages, implying that the TME significantly affected the infiltrating macrophages (Figure S7B). In addition, both resident macrophages and CD1c^{+} DCs were identified in Ma et al.'s datasets[30] (Figure S7C), indicating that resident macrophages are recurrent in different patients.

We also compared the differentially expressed genes in macrophage clusters between the peri-tumoral and tumoral sites (Figure S7D). Tumoral-resident macrophages showed more characteristics of antigen

Figure 3. Dedifferentiation and proliferation state of ICC malignant cells reflect poor clinical outcomes

(A) The Kaplan-Meier plotter analysis was performed to investigate the correlation between patients' prognosis and the dedifferentiation/proliferation status of malignant cells. This analysis was based on the GSEA score of dedifferentiation/proliferation. The results of the analysis provide insights into the impact of the dedifferentiation/proliferation status on patient survival. (B) A box plot was generated to illustrate the relationship between the dedifferentiation/proliferation state of the malignant cells and the dedifferentiation/proliferation GSEA score. The plot provides a visual representation of the distribution and statistical characteristics of the GSEA scores across different states of dedifferentiation/proliferation. (C) The heatmap provides a comprehensive overview of protein expression levels across 110 ICC tumor specimens. It visually represents the relative expression levels of proteins using a color key ranging from blue to red. (D) The Kaplan-Meier survival curve was generated to analyze the prognosis of each malignant subgroup based on the dedifferentiation/proliferation GSEA score using our in-house proteomics datasets. This analysis provides insights into the impact of the dedifferentiation/proliferation status on the survival outcome in ICC. (E) A heatmap was generated to visualize the protein expression levels in our in-house proteomics datasets. The heatmap provides a comprehensive overview of the relative expression levels of proteins in ICC tumor tissues, with the color key ranging from blue to red indicating the relative expression levels of proteins, from low to high. Groups can be divided into group 1 (dedifferentiation[high] and proliferation[high]), group 2 (dedifferentiation[high] and proliferation[low]), group3 (dedifferentiation[low] and proliferation[low]), and group4 (dedifferentiation[low] and proliferation[low]). (F) GO analysis was conducted to explore the biological activities associated with different groups based on the dedifferentiation/proliferation GSEA score. This analysis provides valuable information about the functional processes and pathways that are enriched in each group, shedding light on the underlying biological mechanisms related to dedifferentiation/proliferation in ICC.
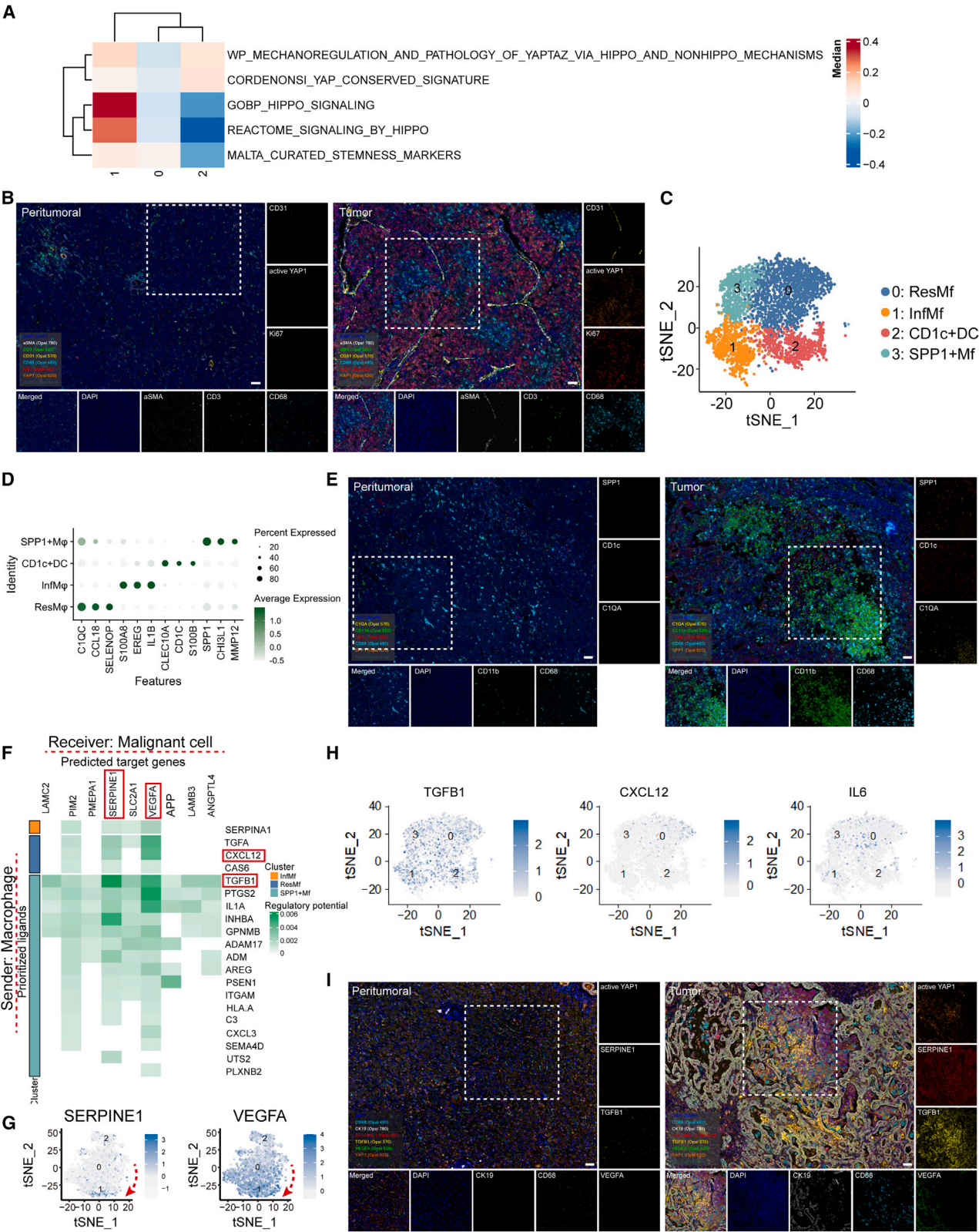
(legend on next page)

presentation and inflammation (Figure S7E). SPP1^{+} macrophages showed more characteristics of extracellular matrix (ECM) remodeling (Figure S7F).

Next, we determined whether the interaction between macrophages and malignant cells was regulated by specific macrophage clusters. NicheNET analysis on macrophages and dedifferentiated malignant cells was performed, modeling intercellular communication by linking ligands of sender cells to target genes of receiver cells.[39] In macrophages, 20 top ligand genes were ranked by their ability to regulate the target genes of epithelial cells (Figure 4F). A few important genes are involved in cancer cell dedifferentiation, including TGFB1[40] from SPP1^{+} macrophages and CXCL12[41] from resident macrophages. These ligands regulate a series of downstream genes involved in the dedifferentiation of malignant cells (Figure 4F), including SERPINE1 and VEGFA, which are associated with tumor cell dedifferentiation.[42,43] In addition, TGFB1 detected in NicheNET analysis was reported to induce malignant cell dedifferentiation through the Hippo signaling pathway.[44] Consistent with the NicheNET analysis, SERPINE1 and VEGFA were enriched in dedifferentiated malignant cultures (Figure 4G). VEGFA is also a downstream gene of the Hippo signaling pathway.[45] We noticed that TGFB1 expression was not restricted to specific macrophage subpopulations, whereas CXCL12 was specific to resident macrophages (Figure 4H). Zhang et al.[46] found that cancer-associated fibroblasts (CAFs) clustered into six subpopulations in ICC tissues and that IL-6^{+} fibroblasts promoted ICC metastasis. However, IL-6 secretion was mainly produced by macrophages, especially C1QA/B[+] resident macrophages (ResMf) and SPP1^{+} macrophages (Figures 4H and S8A).

To validate the NicheNET analysis, we performed mIHC analysis of ICC tumor samples. We noticed that the KRT19^{+} epithelial cells of the peritumoral sample were devoid of Hippo signaling, as represented by the staining of the key transcription factor YAP1, which belongs to the Hippo signaling pathway. In contrast, the active YAP1^{+} malignant cells were surrounded by TGFB1^{+} CD68^{+} macrophages. Consistent with NicheNET analysis, SERPINE1 and VEGFA were also detected in the surrounding active YAP1^{+} malignant cells (Figure 4I). Notably, our mIHC staining showed that TGFB1 staining overlapped with active YAP1. Next, we performed t-SNE analysis to demonstrate the expression of YAP1 and TFGB1 in scRNA-seq and found that the expression of TGFB1 was not significantly associated with YAP1 in a single cell state (Figure S8B). To further verify this result, we split all cells in our mIHC staining and used t-SNE analysis to show the expression of each selected gene, which showed that macrophages might regulate the dedifferentiation of ICC cells by activating YAP1 and regulating the expression of SERPINE1 and VEGFA by upregulating TGFB1 (Figures S8C and S8D). In addition, the western blot results were consistent with those of our mIHC staining (Figure S8E).

We further investigated the effects of macrophages on proliferating malignant cells. NicheNET analysis revealed that the 12 top-ranked ligand genes from macrophages were ordered according to their activity in regulating the target genes of proliferating malignant cells (Figure S9A). The most significant ligand was high-mobility group B2 (HMGB2). These ligands regulate a series of downstream genes in epithelial cells, such as cell-cycle control genes CCNB1, CENPE, CENPF, MKI67, and NCAPG, and a gene associated with cell division, TOP2A (Figures S9A and S9B). Our t-SNE analysis showed that HMGB2 was expressed in these four subcluster macrophages, and the expression of HMGB2 was significantly related to poor patient survival (Figures S9C and S9D).
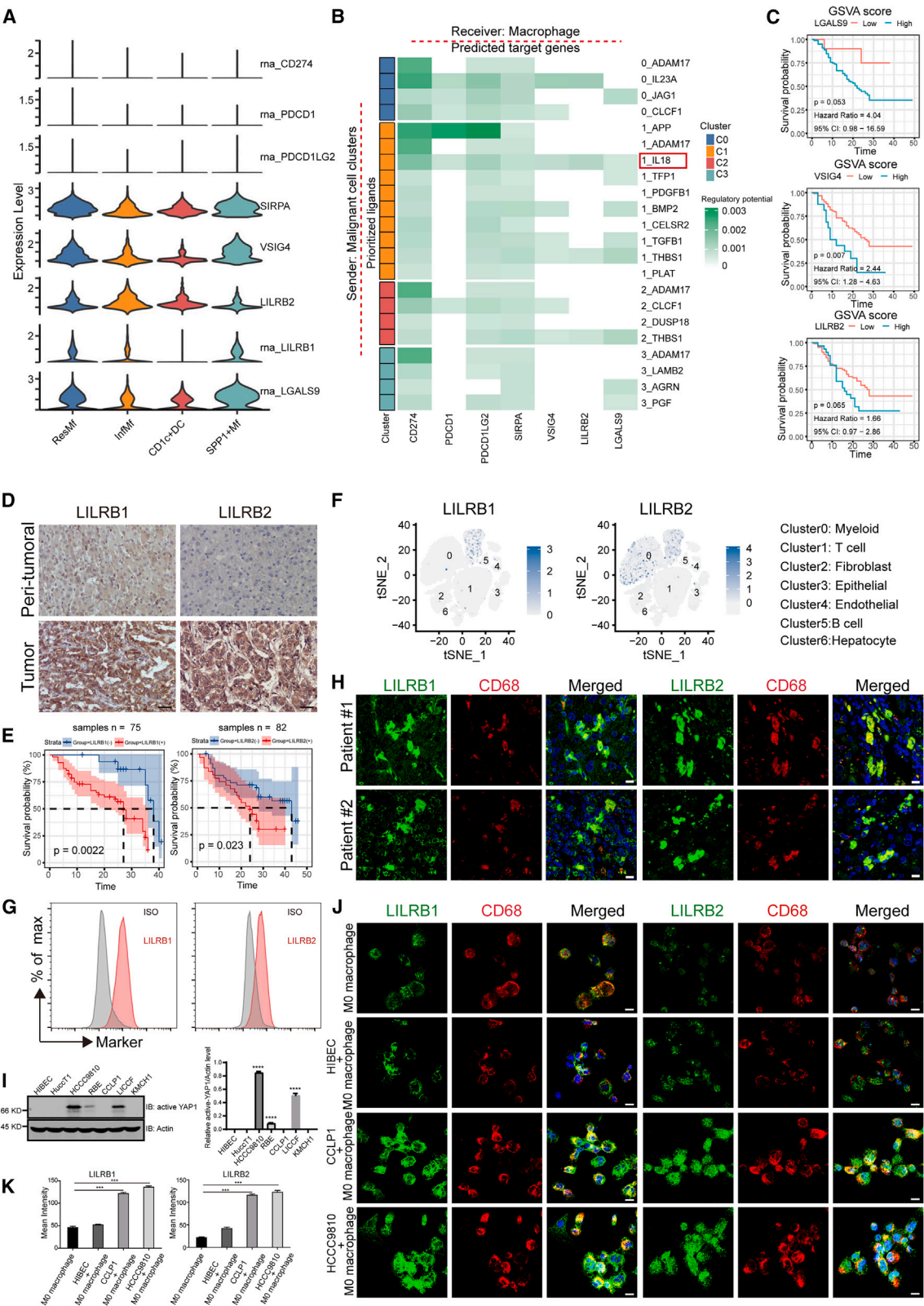
To validate the interaction between macrophages and proliferating malignant cells, we first knocked down the HMGB2 gene in the THP-1 monocytic cell line using short hairpin RNA (shRNA) (Figure S9E) and induced the cell into M0 stage by phorbol 12-myristate 13-acetate (PMA).[47] The induced macrophages were then cocultured with CCLP1, an ICC cell line. HMGB2 knockdown (KD) in macrophage led to less proliferative ICC cells in vitro (Figures S9F and S9G).

mIHC analysis was also performed for ICC tumor samples to validate the macrophage-proliferating malignant cell interaction. We observed Ki67^{+} malignant cells surrounding the HMGB2^{+} CD68^{+} macrophages (Figure S9H).

Taken together, our data show that macrophages play a critical role in promoting the dedifferentiation and proliferation of malignant cells.

Figure 4. Macrophages promote malignant cell dedifferentiation and proliferation

(A) The heatmap demonstrates the enrichment of signaling pathways in three different malignant subsets based on GSVA score. The color key ranging from blue to red represents the GSVA analysis score, indicating the degree of enrichment from low to high. (B) mIHC was conducted on ICC tumor samples to validate the activation of the Hippo signaling pathway. The staining included CD31 for endothelial cells, CD68 for macrophages, CD3 for T cells, and αSMA for fibroblasts. The scale bar represents 50 μm. (C) A t-SNE plot was employed to identify four distinct cell types within the macrophage population: CD68^{+} CD11b^{low} C1QA/B^{+} resident macrophages (ResMf), CD68^{+} CD11b^{+} infiltrating macrophages (InfMf), SPP1^{+} macrophages (SPP1+ Mf), and CD1c+ DCs. (D) The heatmap illustrates the expression levels of specific markers in each macrophage subpopulation. The color key ranging from gray to green represents the average expression levels from low to high. (E) mIHC analysis was performed on ICC tumor samples to validate the existence of the four macrophage cell types identified earlier. The staining included CD68 and C1QA for resident macrophages, CD68 and CD11b for infiltrating macrophages, SPP1 for SPP1+ macrophages, and CD1c for CD1c+ DCs. The scale bar represents 50 μm. (F) Ligand-target gene interactions between macrophages and epithelial cells were examined. The heatmap displays the regulatory potential, with the color key ranging from gray to green indicating the degree of potential regulation from low to high. (G) t-SNE plots demonstrate the expression levels of SERPINE1 (left) and VEGFA (right) in different malignant cell subgroups based on scRNA-seq. The color key ranging from gray to blue indicates the relative expression levels from low to high. (H) A t-SNE plot was generated to visualize the expression levels of TGFB1, VEGFA, and IL-6 in different macrophage subpopulations based on scRNA-seq. The color key ranging from gray to blue indicates the relative expression levels from low to high. (I) mIHC staining on ICC tumor samples was conducted to validate the findings of the NicheNET analysis. The staining included CD68 to identify macrophages, and the analysis suggested that CD68 might regulate malignant cells through overexpressed TGFB1 and activated YAP1. The scale bar represents 50 μm.

A

B Receiver: Macrophage — Predicted target genes

C GSVA score

D

E samples n = 75   samples n = 82

F Cluster0: Myeloid
Cluster1: T cell
Cluster2: Fibroblast
Cluster3: Epithelial
Cluster4: Endothelial
Cluster5: B cell
Cluster6: Hepatocyte

G

H

I

J

K

(legend on next page)

Malignant cells induce immunosuppressive macrophages

We suggest that macrophages could induce malignant cell dedifferentiation and proliferation in the previous sections, and we investigated whether epithelial cells play a role in regulating the function of macrophages.

As TAM is an important immunosuppressive player, we performed NicheNET analysis between malignant cells and macrophages to identify potential interactions shaping the immunosuppressive TME.

A list of immune checkpoints expressed by TAM was set as the genes of interest (GOIs) (Figure 5A), including *PDCD1*, *PDCD1LG2*, *VSIG4*, *LILRB1/2*, *CD274*, *SIRPA*, and *LGALS9*.[48–53] The potential of the ligand on each malignant cell cluster to induce GOI was calculated using NicheNET (Figure 5B). Most interactions between malignant cells and macrophages were induced by dedifferentiation of malignant cells (cluster 1) (Figure 5B). Three out of seven induced immune checkpoints, including VSIG4, LILRB2, and LGALS9, were associated with worse patient prognosis, based on proteomic data (Figure 5C).

LILRB1/2 is a promising immune-regulating gene family[54] that was characterized further. Both LILRB1 and 2 expressions were higher in the tumoral region than in the peritumoral region (Figure 5D). Pathological examination of our collection of ICC patients showed that LILRB1/2 high patients exhibited a worse prognosis (Figure 5E; Table S7). LILRB1/2 was expressed by TAM in the ICC TME (Figure 5F) based on scRNA-seq analysis. LILRB1/2 expression was validated by fluorescence-activated cell sorting (FACS) and immunofluorescence (IF) assays (Figures 5G, 5H, and S10A).

To verify LILRB1/2 induction by malignant cells, THP-1 cells were first induced to M0 stage by PMA[47] and then cocultured with active YAP1+ ICC cell lines CCLP1 and HCCC9810 (Figure 5I). LILRB1/2 signal increased when cocultured with both cell lines, which was consistent with NicheNET analysis that LILRB1/2 could be induced

by active YAP1+ dedifferentiation of malignant cells (Figures 5J and 5K). In addition, we verified the induction mode using a co-culture experiment with malignant cells and macrophages. IL-18 was suggested to induce myeloid checkpoints based on NicheNET analysis (Figure 5B). ICC produced significant levels of IL-18 (Figure S11A). We found that LILRB1/2 induction by ICC cells decreased when IL-18 was blocked by the VX-765 inhibitor (Figures S11B and S11C).

Overall, we found that malignant cells could induce immunosuppressive TAM through the expression of a series of immune checkpoints, thus shaping the ICC TME into an immunosuppressive state.

ICC mouse model recapitulates human findings

Next, we established a mouse ICC model to validate the major findings from human datasets. Based on previous studies, targeting CD169+ Kupffer cells shows potential as a novel immunotherapy for HCC.[35] Thus, we injected control mice and *CD169-DTR* mice[55,56] with the plasmid mixture per mouse, including pT3-EF1a-NICD, PT3-myr-AKT-HA, and pCMV-CAT-T7-SB100, by hydrodynamic transfection to construct an ICC model of carcinoma *in situ*.[57,58] After 1 week, diphtheria toxin (DT) was injected intraperitoneally twice a week for 3 weeks. After a total of 4 weeks, the mice were analyzed by HE, FACS, mIHC, and IHC staining (Figure 6A).

scRNA-seq was performed for both groups (Figure 6A). Nine major cell populations were identified (Figures 6B and 6C). Cell identification was performed using SingleR with manual assistance. A typical marker for each population is shown in Figure 6D and Table S8. Mouse macrophages were further refined and five macrophage clusters were observed (Figures 6E and 6F; Table S9), and the feature genes of each subgroup are shown in Table S10. The four major human ICC myeloid cells, including resident macrophages, SPP1+ macrophages, and infiltrating macrophages, were conserved in mice (Figure 6G). Using mIHC, we showed that resident macrophages (C1QA), SPP1+ macrophages (SPP1), infiltrating macrophages (CD11b), and CD1c+ DCs (CD1c) were present 1 week after tumor

---

Figure 5. Malignant cells induce immunosuppressive macrophages

(A) A list of immune checkpoints expressed by TAM was set as GOI. Violin plot showed the expressions of seven GOI immune checkpoints in macrophages based on feature genes from four subcluster macrophages. (B) The interaction potential between the ligands on each malignant cell cluster and the GOIs of macrophages were examined. Using a color key ranging from gray to green, the interaction potential was visualized, with green indicating high interaction potential and gray indicating low interaction potential. (C) To evaluate the prognostic significance of immune checkpoint expression in patients with ICC, a Kaplan-Meier survival curve was constructed based on proteomic data from our in-house cohort of 110 patients with ICC. The *p* values obtained from two-sided log rank tests were used to assess the statistical significance of the survival differences. (D) IHC staining was performed to examine the expression of two immune checkpoints, LILRB1 and LILRB2, in peritumoral tissues (adjacent normal tissues) and ICC tissues. The staining results were visualized using a scale bar, and a magnification of 40 μm was used. (E) Kaplan-Meier survival curve of LILRB1 (left, *p* = 0.03, hazard ratio, 0.35; 95% confidence interval [CI]:, 0.14–0.91) and LILRB2 (right, *p* = 0.078, hazard ratio, 0.39; 95% CI, 0.14–1.11) expression in patients with ICC (from our own collection). *p* values were obtained from two-sided log rank tests. (F) t-SNE plots were generated to visualize the expression levels of LILRB1 and LILRB2 in the tumor TME of ICC. The color key ranged from gray to blue, with blue indicating high expression levels and gray indicating low expression levels. (G) Flow cytometry analysis was performed to confirm the expression of LILRB1 and LILRB2 by TAM in the TME of ICC. The results showed that TAM indeed expressed these immune checkpoints. (H) IF staining was used to further validate the expression of LILRB1 and LILRB2 by TAM in patients' samples. CD68 was used to label macrophages, and a scale bar representing 10 μm was used to visualize the staining results. (I) Western blot assay was conducted to compare the expression of active YAP1, a downstream signaling molecule, in a normal bile duct epithelial cell line (HIBEC) and several ICC cell lines. For the statistical analysis of active YAP1/actin level, ****p* < 0.0001. (J and K) IF showed the LILRB1/2 staining. In brief, 80 nM PMA was used to induce THP-1 cell to M0 macrophages and incubated for 48 h then directly co-cultured with normal bile duct epithelial cell line HIBECs and ICC cell line CCLP1 and HCCC9810 for another 24 h. Scale bar, 10 μm ***p* < 0.001. All experiments were independently repeated more than three times to ensure reproducibility.
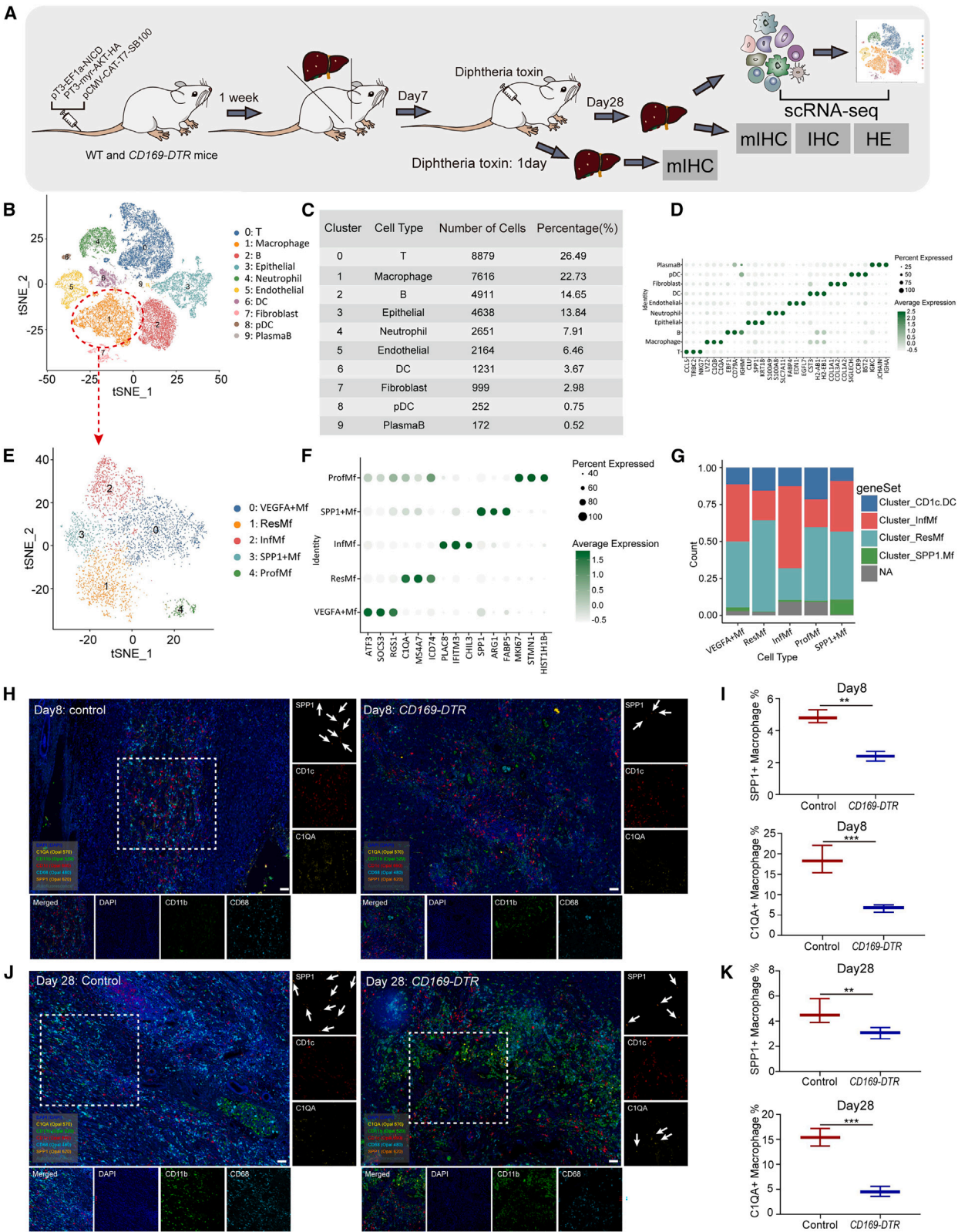
(legend on next page)

induction (Figures 6H and 6I). After 3 weeks of depletion, the ablation effect persisted until day 28 (Figures 6J and 6K). We observed that resident macrophages and SPP1$^+$ macrophages were the major targets in *CD169-DTR* mice (Figures 6H and 6K).

Thus, macrophage subsets identified in human scRNA-seq datasets can also be found in the mouse ICC model. In addition, the key players in immunosuppression and dedifferentiation, resident macrophages and SPP1$^+$ macrophages, could be depleted in *CD169-DTR* mice.

Dedifferentiation-immunosuppression loop disruption for ICC treatment

Next, we disrupted the dedifferentiation-immunosuppression loop between malignant cells and macrophages as a novel ICC treatment strategy.

First, we assessed the tumor tissues by HE staining and found that the number of lesions was significantly reduced in *CD169-DTR* mice (Figures 7A and 7B). Macrophage depletion efficiency was verified by FACS (Figures 7C and 7D).

After macrophage depletion (F4/80 staining), proliferating malignant cells in *CD169-DTR* mice were also reduced (Figures 7C and 7F), and the TGFB1 signal was decreased (Figures 7E and 7F). In addition, the dedifferentiation of malignant cells (active YAP1$^+$) was reduced (Figures 7E and 7F). Similar to the human results, mouse malignant epithelial cells could be identified from epithelial cells (Figures 7G and 7H). We also observed the basal, differentiation, and proliferation states in mice (Figures 7I and 7J). Consistent with the IHC results, we observed a reduction in the number of proliferating and dedifferentiated malignant cell clusters (Figure 7K).

Next, we observed the T cell response after disruption of the dedifferentiation-immunosuppression loop. The gating strategies for the T cells are shown in Figure S12A. We found that the total number of T cells and antitumor CD8$^+$ T cells increased (Figures S12B and S12C), whereas PD-1$^+$ CD8$^+$ T cells decreased in macrophage-depleted tumors (Figures S12D and S12E).

Our results suggest that disruption of dedifferentiation-immunosuppression through TAM targeting could decrease both proliferation and dedifferentiation of malignant cells and enhance the antitumor T cell response. Disruption of dedifferentiation-immunosuppression could be used as a novel immunotherapy for ICC treatment (Figure 8).

DISCUSSION

In this study, we depicted the landscape for both the TME of ICC through scRNA-seq, proteomic, and mIHC analyses and identified malignant cells, stromal cells, and various immune cells of the ICC ecosystem. Importantly, we found decoupled dedifferentiation and proliferation of malignant ICC cells, both of which could be promoted by TAM. On the other hand, malignant cells can induce an immunosuppressive state of TAM, forming a dedifferentiation-immunosuppression loop between malignant cells and TAM. We validated the disruption of dedifferentiation-immunosuppression through TAM targeting, which could be used as a novel immunotherapy for ICC treatment. However, the identification of these two types of developmental pathways is currently only a speculation based on algorithms and lacks the necessary experimental verification. The cells in the proliferative pathway might be more sensitive to chemotherapy due to their active division state, and the dedifferentiated ICC cells could be associated with chemotherapy resistance. This difference in characteristics between the two potential cell states further emphasizes the importance and complexity of precisely classifying and studying malignant tumor cells.

Zhang et al.[46] found that CAFs clustered into six subpopulations in ICC tissues and that IL-6$^+$ fibroblasts promoted ICC metastasis through the IL-6 axis. We noticed that IL-6 secretion was mainly produced by macrophages; thus, such speculation may need to be addressed further in macrophages.

Both KRT18 and TM4SF4 have been reported to be associated with poor prognosis in several types of cancer, including lung, colon, liver, and prostate cancer.[59–61] However, we noticed malignant cell dedifferentiation within the ICC TME accompanied by the downregulation of these malignant markers. Patients enriched with dedifferentiated malignant cell clusters showed worse prognosis.

Figure 6. Mouse scRNA-seq recapitulates human findings

(A) The schematic diagram illustrates the process of establishing the ICC mouse model in wild-type (WT) mice and *CD169-DTR* mice. This model allows for the study of ICC progression and characterization of specific cell types involved. (B) t-SNE) plot was generated to identify the main cell types present in the ICC mouse model. This plot visualizes the clustering of cells based on their gene expression profiles, helping to identify distinct cell populations. (C) The numbers and percentages of assigned cell populations were determined using scRNA-seq data from mouse tumoral tissues. This analysis provides insights into the composition of different cell populations within the ICC model. (D) A heatmap displays the expression levels of feature genes in each cell population. Each cell population is represented by a column, and the expression levels of specific genes are indicated by different shades of green, with darker shades indicating higher expression levels. (E) t-SNE plot was generated to identify subclusters of macrophages within the ICC mouse model. This analysis helps to further characterize the heterogeneity of macrophages and their distinct gene expression profiles. (F) A heatmap highlights the expression levels of feature genes within each subcluster of macrophages. Similar to the previous heatmap, different shades of green indicate the relative expression levels of specific genes in each subcluster. (G) A 100% stacked bar chart illustrates the conservation of four major macrophage subtypes identified in human ICC within the mouse ICC model. This analysis suggests that similar macrophage populations are present in both human and mouse ICC. (H and J) mIHC staining was performed on mouse ICC samples to validate the presence of the four identified macrophage subtypes observed in human ICC scRNA-seq datasets. These mIHC images confirm the presence of these specific macrophage populations in the mouse model. (I and K) Box plots reveal the percentages of SPP1+ and C1QA+ macrophages in the samples shown in (H) and (J), respectively. Three random fields of view were selected for statistical analysis, providing quantitative data on the expression levels of these specific markers within the macrophage populations. **$p < 0.01$, ***$p < 0.001$.
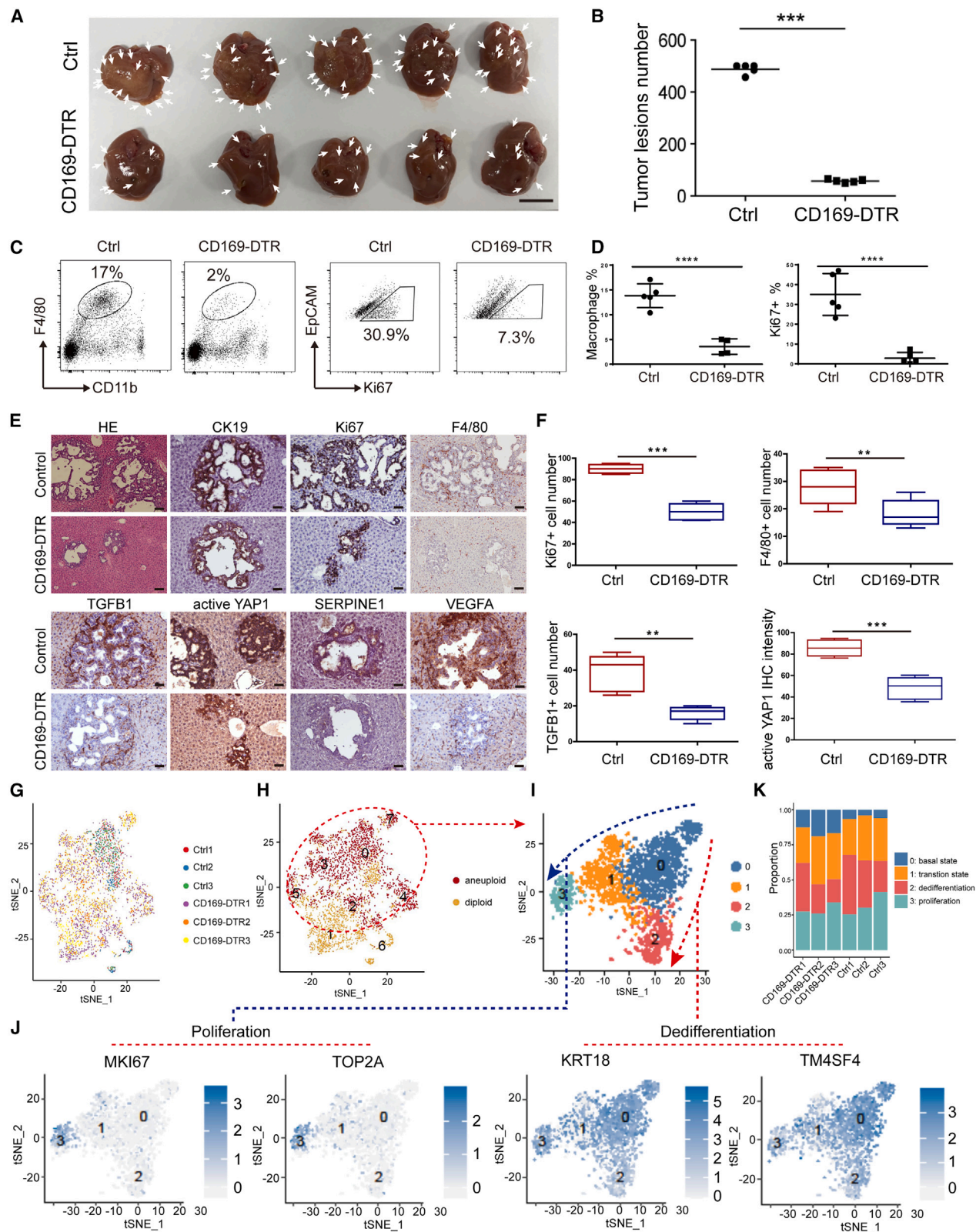
(legend on next page)

Based on cell-cell interaction analysis of macrophages and malignant cells in ICC, we demonstrated the potential role of YAP and HMGB2 in regulating the dedifferentiation and proliferation properties of malignant cells. Our results are consistent with a previous report that YAP promotes colorectal cancer cell dedifferentiation.[62] In addition, Zhang et al. reported an important role of YAP in oncogenic activity in cholangiocarcinoma very recently.[63] HMGB2 functions as a transcriptional activator by modulating chromatin structure and has been shown to play a key role in the regulation of stemness.[64] Our single-cell data suggested that HMGB2 acts as a ligand from macrophages to regulate the proliferation of malignant cells. The downstream regulators in epithelial cells involve several genes involved in the cell cycle and cell proliferation, assisting the malignant cell dedifferentiation process. Furthermore, the above process was confirmed in our mouse model. Depletion of macrophages resulted in a significant decrease in proliferation and malignant cells.

PD-L1 (CD274) is a key immune checkpoint inhibitor expressed by many cancer cells, including ICC cancer cells and myeloid cells, such as TAMs and myeloid-derived suppressor cells.[65–67] However, we noticed PD-L1 expression mainly in mast cells, whereas other myeloid cells and cancer cells expressed low levels of PD-L1. Additionally, we showed that the suppressive ICC TME was mainly shaped by TAMs through other immune checkpoint inhibitors such as LILRB1 and LILRB2. Patients with high levels of LILRB1 and LILRB2 had shorter survival times.

In conclusion, our findings present a comprehensive multi-omics profiling of the ICC TME as a valuable resource for novel biomarkers and therapeutic target discovery based on the dedifferentiation-immunosuppression loop hypothesis. A dedifferentiation-immunosuppression loop disruption strategy was developed to enhance T cell responses against tumors and showed great potential as macrophage-based immunotherapy in ICC treatment.

MATERIALS AND METHODS
Patients and samples
This study used resected ICC samples from 110 patients between 2016 and 2020 at the Affiliated Hospital of Southwest Medical University (Luzhou, China) and NanFang Hospital of Southern Medical University (Guangzhou, China). Ethical approval was obtained from the Medical Ethics Committees of both institutions (Affiliated Hospital of Southwest Medical University, approval no. KY2019053; NanFang Hospital of Southern Medical University, approval nos. NFEC-2021-067 and NFEC-2018-028). Tumor and peritumor samples were acquired from biopsies of six patients with ICC (Table S1) and selected for sequencing using BD Rhapsody and bioinformatics analysis. Histopathological diagnoses and TNM stages of all samples in this study were verified by pathology, and IHC data for LILRB1/2 were interpreted by pathology. Clinical details are presented in Table S2. Overall survival (OS) is defined as the time from surgery to death.

scRNA-seq
GenChem (Shanghai, China) supplied the scRNA-seq service to the ICC tissues. ICC tissue enzymatic digestion was initiated at 37°C for 45 min using 1 mg/mL collagenase I (Worthington) and 1 U/mL of DNase I (Worthington). Subsequently, the cells were filtered through a 70-μm strainer and centrifuged at $300 \times g$ for 5 min to isolate single cells. After discarding the supernatant, red blood cells were lysed in red blood cell lysis buffer (Miltenyi Biotec). The cell pellets were purified by passing through a 40-μm strainer following suspension in $1 \times$ PBS with 0.04% bovine serum albumin (BSA). Library construction and the subsequent steps were performed according to the BD Rhapsody protocol. Single-cell suspensions were randomly distributed in >200,000 microtiter wells for single-cell capture. Oligonucleotide barcode-labeled beads were then introduced into each microwell until saturation. The addition of cell lysis buffer facilitated the hybridization of poly adenylated RNA molecules to these beads. After collection in a tube, the beads were subjected to reverse transcription to convert RNA into cDNA. Each cDNA molecule received a unique molecular identifier (UMI) and a cell label at the 5′ end, marking its origin. This setup utilized the BD Rhapsody protocol for single-cell whole-transcriptome amplification (WTA), starting with the synthesis of the second cDNA strand and proceeding with ligation of the WTA adaptor for amplification across 18 PCR cycles. To prepare sequencing libraries, random priming PCR was employed on the amplified products to enrich for the 3′ ends of transcripts, incorporating both the UMI and the cell label. Library quantification was conducted and each sample library was then sequenced on an Illumina sequencer (Illumina, San Diego, CA, USA) over a 150-bp paired-end cycle, ensuring detailed transcriptional profiling.

Figure 7. Dedifferentiation-immunosuppression loop disruption for ICC treatment
(A and B) The assessment of tumor lesions in control mice versus treated mice was conducted. The error bars represent the SEM, with a sample size of five ($n = 5$). It was observed that, after injecting the plasmids mixture for a period of 4 weeks, numerous small, white, cyst-like lesions appeared on the majority of normal liver tissues. To quantify the tumor burden, the number of lesions on the liver surface was counted. If the count exceeded 500, it was recorded as 500 for each mouse. (C and D) Flow cytometry analysis was performed on macrophages and Ki67 positive epithelial cells. The error bars in this analysis also represent the SEM, with a sample size of five. (E) HE and IHC staining were performed on ICC tissues from control mice and *CD169-DTR* mice. The scale bar for HE staining was set at 100 μm, while for IHC it was set at 40 μm. (F) Box plot was used to display the number of Ki67⁺ cells, F4/80⁺ cells, and TGFB1⁺ cells per 100 cells, as well as the IHC intensity of active YAP1 in the IHC staining. For statistical analysis, five randomly selected fields of view were utilized to obtain accurate results. All IHC statistical data were counted from these five randomly selected fields of view. (G) t-SNE plot was then employed to identify the main cell populations in ICC from our mouse scRNA-seq analysis. (H and I) t-SNE plot identifies malignant cells and aneuploid cells in epithelial cells from our mouse scRNA-seq. (J) t-SNE plots for the expression levels of proliferative cell markers (MKI67 and TOP2A) and malignant cell markers (KRT18 and TM4SF4) in malignant cell subcluster from our mouse scRNA-seq. The color key in these plots indicates the relative expression levels, with gray representing low expression and blue representing high expression. (K) A 100% stacked bar chart was used to illustrate the distribution of the three subgroups of malignant cells identified in our mouse scRNA-seq analysis.

Figure 8. Graphic model of dedifferentiation-immunosuppression loop formed by malignant cell and macrophage in ICC

Malignant cells and macrophages in ICC are involved in a dedifferentiation-immunosuppression loop. Briefly, macrophages play a crucial role in this process by secreting TGFB1, which induces dedifferentiation of malignant cells. This is achieved through the activation of Hippo signaling pathways and the upregulation of SERPINE1 and VEGFA expressions. Additionally, macrophages promote malignant cell proliferation by influencing the expression of HMGB2. In turn, malignant cells reciprocate the interaction by inducing an immunosuppressive TAM phenotype. This is accomplished by the expression of various immune checkpoints, such as LILRB1/2, which contribute to immune evasion and suppression within the TME.

scRNA-seq processing

Preprocessing of the raw gene expression data were accomplished using version 2.3.4 of the Seurat R package. Cells deemed low quality, exhibiting fewer than 200 genes per cell, fewer than three cells per gene, or more than 10% mitochondrial genes, were excluded. Normalization and scaling procedures were applied to the gene expression matrix of cells that met the quality criteria. Highly variable genes were identified using Seurat's default settings and then subjected to principal-component analysis (PCA) to discern significant principal components for further analysis. t-SNE was applied for dimension reduction, and a graph-based algorithm was used for cell cluster determination. Feature genes for each cluster were determined using the Seurat package's "FindAllMarkers" function, applying default settings to define the gene set of each cluster. The gsva package was utilized to

conduct single-sample gene set enrichment analysis (ssGSEA), employing the relevant gene set.

Cell-cell interaction analysis using NicheNET

We used NicheNET to analyze cell-cell interactions.[39] Gene expression data from interacting cells was input into NicheNET and then combined with a pre-existing model incorporating known ligand-to-target signaling pathways. This approach facilitated the prediction of ligand-receptor interactions, highlighting the drivers of gene expression changes within the cells under study.

InferCNV analysis

To determine the somatic large-scale chromosomal copy number variation (CNV) score for cells based on our scRNA-seq, we utilized the InferCNV R package (version 1.6.0). The required raw count

matrix was prepared according to the data requirements outlined in the InferCNV GitHub repository (https://github.com/broadinstitute/inferCNV). CD8+ T cells were chosen as the reference for normal cell conditions in our analysis. Utilizing the default settings recommended by InferCNV (with a cutoff of 0 and denoise set to 0.2), we calculated the CNV score for each cell. This score was derived as the quadratic sum of all the identified CNV regions, enabling a quantified representation of chromosomal instability within individual cells.

CopyKAT analysis

To separate malignant cells from normal cells within our scRNA-seq dataset, we utilized CopyKAT software to assess CNV level.[25] The gene expression matrix of the UMI of our scRNA-seq data served as the input for the copyKAT. The software processed the UMI data and clustered the cells, with an initial focus on confidently identifying the diploid cells. Hierarchical clustering techniques were used to isolate tumor cells based on their distinct CNV differences from normal cells. In cases where the genomes appeared indistinctly different, a Gaussian mixture model (GMM) was used for accurate identification. This methodology enabled the extraction of distinct gene expression profiles for both malignant and normal cells, thus enriching our insights into cellular dynamics within the TME.

RNA velocity of single cells

The study utilized RNA velocity[68] to examine both the pace and trajectory of transcriptomic alterations, hypothesizing that the dynamics of gene splicing and mRNA degradation could be differentiated through the proportion of unspliced to spliced mRNA within an hourly time frame.

Pseudo-time analysis

The Monocle 2 R package was utilized to conduct pseudo-time trajectory analysis, which uncovered the dynamic alterations in the transcriptome of a specific cell lineage during its development. The cells were subjected to dimensional reduction using the DDRTree method, followed by sequencing based on pseudo-time. Finally, the cells were ordered in a manner that allowed the visualization of the developmental trajectory.

GSVA

The GSVA is a commonly employed unsupervised non-parametric method. It aims to estimate the variations in gene set enrichment within gene expression data. This technique is particularly valuable for exploring the activity of pathways and biological processes across different samples in an expression dataset. This research utilized the GSVA R package to validate genomic data derived from GSEA. A p value of less than 0.05 was established as the criterion for statistical significance.

In-house tandem mass tag-based proteomic analysis

In our previous study, we established an ICC-proteomics cohort that incorporating 110 patients.[69] We conducted tandem mass tag (TMT)-based proteomic analyses of formalin-fixed paraffin-embedded (FFPE) specimens. The procedure began with dewaxing and rehydration of the slides, followed by acidic hydrolysis using formic acid.

A solution containing 6 M urea and 2 M thiourea (both from Sigma-Aldrich, Germany) was employed for protein denaturation. Subsequently, proteins were segmented into peptides by trypsin and Lys-C (both from Hualishi, China). Peptides were then labeled using the TMTpro 16 plex kit (Thermo Fisher Scientific, San Jose, USA), with each batch including 15 experimental samples and a single pooled reference sample. Offline high-pH reversed-phase fractionation with a Thermo Dionex Ultimate 3000 RSLCnano System separated the peptides. The fractionated samples were evaluated using a Q Exactive HF mass spectrometer (Thermo Fisher Scientific, San Jose, USA) in DDA mode. Proteome Discoverer software (version 2.4, Thermo Fisher Scientific, Waltham, MA) enabled extensive proteome analysis of ICC in the cohort by searching against a database of reviewed human UniProt entries.

Animal studies

Wild-type (WT) C57BL/6 mice were acquired from GemPharmatech (Nanjing, China). As previously mentioned,[35] *CD169-DTR* mice were created. The Institutional Animal Care and Use Committee approved the Zhejiang Academy of Medical Sciences SPF facility to house the mice in this study. Animal studies were performed in accordance with the National Institutes of Health Guide for the Care and Use of Laboratory Animals.

To establish spontaneous ICC, as previous reported,[70] a plasmid mixture consisting of pCMV-CAT-T7-SB100, pT3-EF1a-NICD, and PT3-myr-AKT-HA was prepared in PBS. The doses were carefully measured to be 20 μg/20 g, 4 μg/20 g, and 1 μg/20 g body weight, respectively. This mixture was then administered into the tail vein of mice on day 1. Following the initial plasmid injection, DT (D0564, Sigma-Aldrich) at a dose of 20 ng/g body weight was injected intraperitoneally into both WT and CD169-DTR mice on day 7. DT injections were repeated every 3 days. On day 28, mice were sacrificed. According to the protocol from Fan et al., many small, white, cyst-like lesions expand in most of the normal liver. The number of lesions was counted to represent the tumor burden. Because the lesions were replaced almost the whole liver, we counted lesions on the liver surface; if the number was more than 500, it was marked as 500. Tumor lesions were collected and analyzed using FACS, IHC, hematoxylin and eosin (H&E) staining, scRNA-seq, and mIHC staining.

Cell lines and culture

The cell lines utilized were acquired from the Cell Bank of the Chinese Academy of Sciences (Shanghai, China). These cell lines were cultivated in a controlled environment, specifically within a CO_2 incubator (Thermo, 3111, US) set to maintain a humidified atmosphere at 37°C. The full growth medium was enriched with fetal bovine serum (FBS) (Gibco, 10% final concentration, US) and penicillin/streptomycin (Thermo Fisher, US) to support optimal cell growth and viability. Distinct media types were used for different cell lines: RPMI-1640 was chosen for the THP1, HCCC9810, and HuCCT1

cell lines, whereas Dulbecco's modified Eagle's medium (DMEM) was selected for the human intrahepatic biliary epithelial cell (HIBEC), CCLP1, LICCF, KMCH1, and HEK293T cell lines.

Stable cell lines

To establish THP1 cell lines with a stable KD of HMGB2, specific shRNA vectors targeting HMGB2 were acquired from Sigma (TRCN0000019010, TRCN0000019011, and TRCN0000019013). HEK293T cells underwent transfection with lentiviral packaging plasmids (pMD2.G and psPAX2) as per the provided guidelines. Subsequently, THP1 cells were exposed to the generated lentiviruses, and cells expressing the shRNAs were enriched using 2 µg/mL puromycin selection. This process incorporated three distinct shRNA sequences. An empty pLKO.1 vector served as the control. The suppression of HMGB2 was confirmed via western blot analysis. Before assessing HMGB2 levels, THP1 cells with the KD construct were exposed to 80 nM PMA (ab120297, Abcam, USA). Throughout the study, THP1 stable cell lines were consistently cultured in a medium containing 2 µg/mL puromycin.

IHC

Tumor tissues resected from ICC patients were fixed with 4% paraformaldehyde (P1110, Solarbio) before embedding in paraffin (YA0012, Solarbio). Tissue samples (4 µm) were treated with xylene to remove paraffin and then gradually rehydrated using increasing concentrations of alcohol. Subsequently, the tissue slices were then blocked with goat serum blocking solution (B900780, Proteintech, China) for an hour, preceding their incubation with the primary antibody throughout the night at 4°C. Antibodies against LILRB1 (ab170909, 1:200, Abcam), LILRB2 (abs139124, 1:100, Abcam), CK19 (ab52625, 1:400, Abcam), Ki67 (550609, 1:400, BD Biosciences), F4/80 (70076S, 1:300, CST), TGFB1 (ab215715, 1:200, Abcam), active YAP1 (ab205270, 1:300, Abcam), SERPINE1 (ab125287, 1:200, Abcam), and VEGFA (ab52917, 1:200, Abcam) were used. The following day, the secondary antibody was applied and incubated for a duration of 0.5 h. The sections were then stained using a peroxidase IHC assay kit (pk10006, Proteintech, China) according to protocol. The slides were then mounted and examined under a Leica light microscope, and the acquired images were analyzed using image analysis software (Image-Pro Plus).

H&E staining

Spontaneous ICC tumor tissues underwent fixation in 4% paraformaldehyde for a day before paraffin embedding. Tissue slices (4 µm) were then deparaffinized in xylene and progressively rehydrated through a series of alcohol dilutions. Following three PBS washes (P1020, Solarbio), the sections were hematoxylin stained (G1080, Solarbio) for half an hour. The slides were then rinsed in PBS and immersed in 1% ammonia water (G1822, Solarbio) to stain the nuclei with blue-violet. The sections were then immersed in 75% alcohol for 2 min and stained with eosin (G1100, Solarbio) for 1 h to stain the cytoplasm. After rinsing with a gradient of alcohol solution, xylene was applied to replace the dehydrated alcohol before mounting. Observations were made under a Leica

light microscope, and images were processed using software (Image-Pro Plus).

mIHC

The experiment was performed using the Opal Polaris 7-color Manual IHC Kit (AKOYA Biosciences, NEL861001KT) for mIHC. Initially, prepared tissue sections of 4 µm were baked at 65°C for an hour. The sections were then dewaxed in xylene and rehydrated using a series of alcohol gradients. Following rehydration, the sections were fixed in 10% neutral buffered formalin (NBF) (G2161, Solarbio, China) for 20 min. Epitope retrieval was performed using an appropriate AR buffer in a microwave, initially at 100% power for 1 min, followed by a lower power setting of 20% for 15 min. After cooling to room temperature, the sections were blocked using the blocking/Ab diluent for 10 min and then incubated with primary antibodies for 10 min. Following primary antibody incubation, the sections were washed three times with 1× TBST (Tris-Borate-Sodium Tween-20) (T1082, Solarbio, China). The Opal Polymer horseradish peroxidase (HRP) Ms+Rb was then applied to the tissue sections for a 10-min incubation. Following another set of three TBST rinses, sections were treated with opal reagent. The above process was repeated. The primary antibodies used in this experiments are provided in Table S3. Next, a complete introduction of Opal TSA-DIG and Opal Polaris 780 labeling was performed. Finally, slides were washed with TBST and distilled water before the nuclei were stained with Mowiol (81381, Sigma-Aldrich) supplemented with DAPI (C1002, Beyotime). Seven-color slides were visualized using the Vectra Polaris Quantitative Imaging System.

mIHC analysis

To elucidate the association between TAM and malignant cells within the TME of ICC, we conducted a comprehensive analysis of mIHC staining using a two-step pipeline.[71] Initially, we utilized a median filter to minimize the noise and enhance the quality of each channel. The median filter had a window size of 5 × 5 to ensure that every output pixel included the median value within its 5-by-5 neighborhood in the input image. Subsequently, we employed a connectivity-aware segmentation method to accurately segment nuclei.[72] Artifacts in other channels were also eliminated if their respective distances to the nearest nucleus centroid exceeded 45 pixels.

Western blotting

Cells were lysed using ice-cold radioimmunoprecipitation assay (RIPA) lysis buffer (R0020, Solarbio) with a protease inhibitor (P6731, Solarbio) and the protein concentration in the lysate was determined using a BCA Protein Assay Kit (P0010S, Beyotime). Proteins were then separated by sodium dodecyl sulfate-polyacrylamide gel electrophoresis (SDS-PAGE) and subsequently transferred onto nitrocellulose membranes (HATF00010, Merck Millipore, USA) for immunoblotting. To prevent non-specific binding, the membranes were blocked for 1 h at room temperature and incubated overnight at 4°C with the following primary antibodies. The next day, after washing three times with PBS with 0.1% Tween 20 (PBST), the membranes were incubated with the secondary antibody for 1 h at room

temperature. After incubation, the membranes underwent additional PBST washes before being visualized on a LI-COR Odyssey imager. Images were quantitatively analyzed using Image Studio software (Version 4.0).

IF staining for tumor tissue
Prepared tissue sections were deparaffinized with xylene and rehydrated with graded alcohol, repaired antigen with microwave heating, permeabilized, and blocked before incubation with primary antibody overnight at 4°C. The next day, the sections were rinsed three times with 1× PBS before staining with Alexa Fluor 488- and 594-labeled fluorescent secondary antibodies (A-11008 and A-11032, Invitrogen, USA) for 1 h at room temperature in the dark, rinsed three times with PBS, and mounted onto slides using Mowoil supplemented with DAPI to stain the nucleus. Finally, ICC samples were imaged using a confocal microscope (Nikon, Japan). Images were analyzed using the ImageJ software (version 4.0).

IF staining for cell culture
IF staining was conducted to observe the differentiation of THP1 cells and their interactions with ICC tumor cells. For the co-culture system, we used the method from Park et al.[73]; THP-1 cells were treated with 80 nM PMA to induce M0 macrophages and seeded into 12-well plates, and the cell number was 1×10^5 per well. After 48 h, 2×10^5 ICC tumor cells were added to the wells for direct co-culture with M0 macrophages. The IF procedure was as follows: cells were rinsed once with cold PBS, fixed with paraformaldehyde for 15 min at room temperature, and cells permeabilized using 0.2% Triton X-100. Following permeabilization, cells were blocked with 2% BSA for 1 h and then labeled with primary antibodies against CD68 (sc-20060, Santa Cruz), LILRB1 (ab170909, Abcam), or LILRB2 (abs139124, Absin) for 1 h. Subsequently, the cells were incubated with the secondary antibodies for 1 h in the dark. Coverslips were washed in PBS three times and then mounted on slides using Mowiol containing DAPI for nuclear staining. Confocal microscopy (Nikon, Japan) was used for cell examination, and ImageJ software (version 4.0) was used for image analysis.

For IL-18 inhibition experiments, after co-culture for 48 h, 0.5 μM VX-765 was added to inhibit the release of IL-18 for another 24 h. IF assays were performed as previously described.

ELISA
The co-culture system was characterized by IF staining. To inhibit the release of IL-18 from ICC tumor cells, the cells were treated with 0.5 μM VX-765 for 24 h. After inhibitor treatment, cell culture supernatants were harvested to detect the concentrations of IL-18 using the Human IL-18 SimpleStep ELISA Kit (ab215539, Abcam) to test the inhibitory effect. Briefly, the cell culture supernatant was collected and centrifuged at $2,000 \times g$ for 10 min to remove debris, and aliquots of 50 μL of prepared samples or standards per well into 96 wells. Next, 50 μL of the cocktail antibody was added and incubated at room temperature for 1 h, followed by washing with 1× wash buffer three times. Next, 100 μL of 3,3′,5,5′-Tetramethylbenzidine (TMB) reagent was added to each well and incubated in the dark for 10 min with

gentle shaking. Finally, 100 μL of stop solution was added and the plate was shaken to mix each well before recording the optical density (OD) at 450 nm. Statistical analyses were performed using the GraphPad Prism software (version 9.3).

FACS in vitro experiment
Co-culture assays were performed as previously described. Initially, THP1 cells were incubated with 80 nM PMA for 48 h to facilitate their differentiation into M0 macrophages, after which they were cocultured with ICC tumor cells. For analysis of surface markers, live cells were resuspended and stained with anti-human CD68 (Y1/82A, 333809, BioLegend) and anti-EpCAM (CO17-1A, 369813, BioLegend) antibodies at 4°C in the dark for 0.5 h. Following this, cells were fixed and permeabilized using the Fixation/Permeabilization Solution Kit (554722, BD Bioscience, USA) for 20 min and then stained with anti-ki67 antibody (11F6, 151206, BioLegend) at 4°C for another 30 min. Data acquisition was performed using an ACEA NovoCyte flow cytometer and analyzed using the FlowJo software (version 10).

FACS
Tissue samples were disaggregated mechanically and enzymatically with 0.6 mg/mL collagenase IV (17104019, Gibco) and 0.01 mg/mL DNase I (11284932001, Merck) at 37°C for 60 min. After digestion, the tissue homogenates were filtered through a 0.4-μm filter (352340, BD Bioscience) to obtain single cells. The cells were then centrifuged at $300 \times g$ for 5 min and resuspended in 36% Percoll buffer. The cell suspension was treated with 10 mL of blood lysis buffer (555899, BD Bioscience) for 10 min at room temperature to eliminate erythrocytes. After lysis, the cells were centrifuged at $300 \times g$ for 5 min and blocked with 2.5 μg/mL Fc blocker (156604, BioLegend) on ice for 10 min. The cells were then incubated with a series of fluorochrome-conjugated antibodies at 4°C for 20 min. Antibodies including Ki67 Alexa Fluor 647 (clone: 11F6; 151206; 1:600; BioLegend), EpCAM-FITC (clone: CO17-1A; 1:600; BioLegend), CD68-FITC (clone: Y1/82A, 1:600, BioLegend), F4/80-PE-Cyanine7 (clone: BM8, 1:600, Invitrogen), CD11b-PE-CF594 (clone: M1/70, 1:600, BD biosciences), EpCAM-Brilliant Violet 510 (clone: G8.8, 1:600, BioLegend), Cd45-BV605 (clone: 30-F11, 1:600, BD biosciences), CD19-BUV395 (clone: 1D3, 1:600, BD biosciences), CD3-FITC (clone: 17A2, 1:600, BioLegend), CD49b- PE Hamster (clone: HMα2, 1:600, BD biosciences), CD4- APC-Cy7 (clone: GK1.5, 1:600, BD biosciences), CD8-PE-Cy7 (clone: 53–6.7, 1:600, BD biosciences), and PD-1-Brilliant Violet 421 (clone: 29F.1A12, 1:600, BioLegend). All primary antibodies used are listed in Table S3. Following incubation, the cells were washed once and resuspended in FACS buffer for subsequent analysis using a five-laser flow cytometer (BD Bioscience, Fortessa). Cell sorting was performed using a MoFlo Astrios EQ Cell Sorter (Beckman Coulter, USA), and flow cytometry data were analyzed using FlowJo software (TreeStar).

Statistical analysis
Raw data were imported into GraphPad Prism. Initial data distribution and variability assessments were used to determined statistical

tests. Two-tailed Student's t tests indicated significant differences between the groups. One-way ANOVA followed by Bonferroni's *post hoc* test was used for analyses involving three or more groups. Results are presented as mean ± standard error of the mean (SEM). The log rank test is used in survival analysis to compare the distribution of time to event in two or more independent samples. Statistical significance was set at $p < 0.05$.

AUTHOR CONTRIBUTIONS
The experiments were executed mainly using J.R., Q.L., Y.J., and C.Y. Data analysis was assisted by J.Y. F.C., S.X., R.C., C.L., J.C., X.B., and X.R. carried out the animal experiments or provided intellectual contributions to this study. The manuscript was edited by H.W., J.S., D.Z., and P.Z. W.F. and M.J. designed the experiments and wrote the manuscript. All authors reviewed the manuscript before submission.

DECLARATION OF INTERESTS
The authors declare no competing interests.

SUPPLEMENTAL INFORMATION
Supplemental information can be found online at https://doi.org/10.1016/j.ymthe.2025.02.019.

REFERENCES
1. Moris, D., Palta, M., Kim, C., Allen, P.J., Morse, M.A., and Lidsky, M.E. (2023). Advances in the treatment of intrahepatic cholangiocarcinoma: An overview of the current and future therapeutic landscape for clinicians. CA Cancer J. Clin. 73, 198–222. https://doi.org/10.3322/caac.21759.

2. Sarcognato, S., Sacchi, D., Fassan, M., Fabris, L., Cadamuro, M., Zanus, G., Cataldo, I., Capelli, P., Baciorri, F., Cacciatore, M., and Guido, M. (2021). Cholangiocarcinoma. Pathologica 113, 158–169. https://doi.org/10.32074/1591-951x-252.

3. Bray, F., Laversanne, M., Sung, H., Ferlay, J., Siegel, R.L., Soerjomataram, I., and Jemal, A. (2024). Global cancer statistics 2022: GLOBOCAN estimates of incidence and mortality worldwide for 36 cancers in 185 countries. CA Cancer J. Clin. 74, 229–263. https://doi.org/10.3322/caac.21834.

4. Kelley, R.K., Ueno, M., Yoo, C., Finn, R.S., Furuse, J., Ren, Z., Yau, T., Klümpen, H.J., Chan, S.L., Ozaka, M., et al. (2023). Pembrolizumab in combination with gemcitabine and cisplatin compared with gemcitabine and cisplatin alone for patients with advanced biliary tract cancer (KEYNOTE-966): a randomised, double-blind, placebo-controlled, phase 3 trial. Lancet 401, 1853–1865. https://doi.org/10.1016/s0140-6736(23)00727-4.

5. Martin-Serrano, M.A., Kepecs, B., Torres-Martin, M., Bramel, E.R., Haber, P.K., Merritt, E., Rialdi, A., Param, N.J., Maeda, M., Lindblad, K.E., et al. (2023). Novel microenvironment-based classification of intrahepatic cholangiocarcinoma with therapeutic implications. Gut 72, 736–748. https://doi.org/10.1136/gutjnl-2021-326514.

6. Greten, T.F., Schwabe, R., Bardeesy, N., Ma, L., Goyal, L., Kelley, R.K., and Wang, X.W. (2023). Immunology and immunotherapy of cholangiocarcinoma. Nat. Rev. Gastroenterol. Hepatol. 20, 349–365. https://doi.org/10.1038/s41575-022-00741-4.

7. Rizvi, S., Khan, S.A., Hallemeier, C.L., Kelley, R.K., and Gores, G.J. (2018). Cholangiocarcinoma - evolving concepts and therapeutic strategies. Nat. Rev. Clin. Oncol. 15, 95–111. https://doi.org/10.1038/nrclinonc.2017.157.

8. Job, S., Rapoud, D., Dos Santos, A., Gonzalez, P., Desterke, C., Pascal, G., Elarouci, N., Ayadi, M., Adam, R., Azoulay, D., et al. (2020). Identification of Four Immune Subtypes Characterized by Distinct Composition and Functions of Tumor Microenvironment in Intrahepatic Cholangiocarcinoma. Hepatology 72, 965–981. https://doi.org/10.1002/hep.31092.

9. Yuan, H., Lin, Z., Liu, Y., Jiang, Y., Liu, K., Tu, M., Yao, N., Qu, C., and Hong, J. (2020). Intrahepatic cholangiocarcinoma induced M2-polarized tumor-associated macrophages facilitate tumor growth and invasiveness. Cancer Cell Int. 20, 586. https://doi.org/10.1186/s12935-020-01687-w.

10. Liu, Y., Xu, Q., Deng, F., Zheng, Z., Luo, J., Wang, P., Zhou, J., Lu, X., Zhang, L., Chen, Z., et al. (2023). HERC2 promotes inflammation-driven cancer stemness and immune evasion in hepatocellular carcinoma by activating STAT3 pathway. J. Exp. Clin. Cancer Res. 42, 38. https://doi.org/10.1186/s13046-023-02609-0.

11. Lin, Y., Cai, Q., Chen, Y., Shi, T., Liu, W., Mao, L., Deng, B., Ying, Z., Gao, Y., Luo, H., et al. (2022). CAFs shape myeloid-derived suppressor cells to promote stemness of intrahepatic cholangiocarcinoma through 5-lipoxygenase. Hepatology 75, 28–42. https://doi.org/10.1002/hep.32099.

12. Bhuria, V., Xing, J., Scholta, T., Bui, K.C., Nguyen, M.L.T., Malek, N.P., Bozko, P., and Plentz, R.R. (2019). Hypoxia induced Sonic Hedgehog signaling regulates cancer stemness, epithelial-to-mesenchymal transition and invasion in cholangiocarcinoma. Exp. Cell Res. 385, 111671. https://doi.org/10.1016/j.yexcr.2019.111671.

13. Yoshino, J., Akiyama, Y., Shimada, S., Ogura, T., Ogawa, K., Ono, H., Mitsunori, Y., Ban, D., Kudo, A., Yamaoka, S., et al. (2020). Loss of ARID1A induces a stemness gene ALDH1A1 expression with histone acetylation in the malignant subtype of cholangiocarcinoma. Carcinogenesis 41, 734–742. https://doi.org/10.1093/carcin/bgz179.

14. Sugiura, K., Mishima, T., Takano, S., Yoshitomi, H., Furukawa, K., Takayashiki, T., Kuboki, S., Takada, M., Miyazaki, M., and Ohtsuka, M. (2019). The Expression of Yes-Associated Protein (YAP) Maintains Putative Cancer Stemness and Is Associated with Poor Prognosis in Intrahepatic Cholangiocarcinoma. Am. J. Pathol. 189, 1863–1877. https://doi.org/10.1016/j.ajpath.2019.05.014.

15. Lamhamedi-Cherradi, S.E., Mohiuddin, S., Mishra, D.K., Krishnan, S., Velasco, A.R., Vetter, A.M., Pence, K., McCall, D., Truong, D.D., Cuglievan, B., et al. (2021). Transcriptional activators YAP/TAZ and AXL orchestrate dedifferentiation, cell fate, and metastasis in human osteosarcoma. Cancer Gene Ther. 28, 1325–1338. https://doi.org/10.1038/s41417-020-00281-6.

16. Aran, D., Looney, A.P., Liu, L., Wu, E., Fong, V., Hsu, A., Chak, S., Naikawadi, R.P., Wolters, P.J., Abate, A.R., et al. (2019). Reference-based analysis of lung single-cell sequencing reveals a transitional profibrotic macrophage. Nat. Immunol. 20, 163–172. https://doi.org/10.1038/s41590-018-0276-y.

17. Buechler, M.B., Pradhan, R.N., Krishnamurty, A.T., Cox, C., Calviello, A.K., Wang, A.W., Yang, Y.A., Tam, L., Caothien, R., Roose-Girma, M., et al. (2021). Cross-tissue organization of the fibroblast lineage. Nature 593, 575–579. https://doi.org/10.1038/s41586-021-03549-5.

18. Lertkiatmongkol, P., Liao, D., Mei, H., Hu, Y., and Newman, P.J. (2016). Endothelial functions of platelet/endothelial cell adhesion molecule-1 (CD31). Curr. Opin. Hematol. 23, 253–259. https://doi.org/10.1097/moh.0000000000000239.

19. Ramboer, E., De Craene, B., De Kock, J., Vanhaecke, T., Berx, G., Rogiers, V., and Vinken, M. (2014). Strategies for immortalization of primary hepatocytes. J. Hepatol. 61, 925–943. https://doi.org/10.1016/j.jhep.2014.05.046.

20. Carvelli, J., Demaria, O., Vély, F., Batista, L., Chouaki Benmansour, N., Fares, J., Carpentier, S., Thibult, M.L., Morel, A., Remark, R., et al. (2020). Association of COVID-19 inflammation with activation of the C5a-C5aR1 axis. Nature 588, 146–150. https://doi.org/10.1038/s41586-020-2600-6.

21. Rosowski, E.E. (2020). Determining macrophage versus neutrophil contributions to innate immunity using larval zebrafish. Dis. Model. Mech. 13, dmm041889. https://doi.org/10.1242/dmm.041889.

22. Ren, J.C., Wang, T., Wu, H., Zhang, G.H., Sun, D., Guo, K., Li, H., Zhang, F., Wu, W., and Xia, Z.L. (2020). Promoter hypermethylation in CSF3R induces peripheral neutrophil reduction in benzene-exposure poisoning. Environ. Mol. Mutagen. 61, 786–796. https://doi.org/10.1002/em.22382.

23. Xie, Z., Niu, L., Zheng, G., Du, K., Dai, S., Li, R., Dan, H., Duan, L., Wu, H., Ren, G., et al. (2023). Single-cell analysis unveils activation of mast cells in colorectal cancer microenvironment. Cell Biosci. 13, 217. https://doi.org/10.1186/s13578-023-01144-x.

24. Lewis, S.M., Treacher, D.F., Edgeworth, J., Mahalingam, G., Brown, C.S., Mare, T.A., Stacey, M., Beale, R., and Brown, K.A. (2015). Expression of CD11c and EMR2 on neutrophils: potential diagnostic biomarkers for sepsis and systemic inflammation. Clin. Exp. Immunol. 182, 184–194. https://doi.org/10.1111/cei.12679.

25. Gao, R., Bai, S., Henderson, Y.C., Lin, Y., Schalck, A., Yan, Y., Kumar, T., Hu, M., Sei, E., Davis, A., et al. (2021). Delineating copy number and clonal substructure in human tumors from single-cell transcriptomes. Nat. Biotechnol. 39, 599–608. https://doi.org/10.1038/s41587-020-00795-2.

26. Patel, A.P., Tirosh, I., Trombetta, J.J., Shalek, A.K., Gillespie, S.M., Wakimoto, H., Cahill, D.P., Nahed, B.V., Curry, W.T., Martuza, R.L., et al. (2014). Single-cell RNA-seq highlights intratumoral heterogeneity in primary glioblastoma. Science 344, 1396–1401. https://doi.org/10.1126/science.1254257.

27. La Manno, G., Soldatov, R., Zeisel, A., Braun, E., Hochgerner, H., Petukhov, V., Lidschreiber, K., Kastriti, M.E., Lönnerberg, P., Furlan, A., et al. (2018). RNA velocity of single cells. Nature 560, 494–498. https://doi.org/10.1038/s41586-018-0414-6.

28. Zhang, H., Chen, X., Wang, J., Guang, W., Han, W., Zhang, H., Tan, X., and Gu, Y. (2014). EGR1 decreases the malignancy of human non-small cell lung carcinoma by regulating KRT18 expression. Sci. Rep. 4, 5416. https://doi.org/10.1038/srep05416.

29. Zhang, F., Ye, J., Guo, W., Zhang, F., Wang, L., and Han, A. (2022). TYMS-TM4SF4 axis promotes the progression of colorectal cancer by EMT and upregulating stem cell marker. Am. J. Cancer Res. 12, 1009–1026.

30. Ma, L., Wang, L., Khatib, S.A., Chang, C.W., Heinrich, S., Dominguez, D.A., Forgues, M., Candia, J., Hernandez, M.O., Kelly, M., et al. (2021). Single-cell atlas of tumor cell evolution in response to therapy in hepatocellular carcinoma and intrahepatic cholangiocarcinoma. J. Hepatol. 75, 1397–1408. https://doi.org/10.1016/j.jhep.2021.06.028.

31. Yimlamai, D., Christodoulou, C., Galli, G.G., Yanger, K., Pepe-Mooney, B., Gurung, B., Shrestha, K., Cahan, P., Stanger, B.Z., and Camargo, F.D. (2014). Hippo pathway activity influences liver cell fate. Cell 157, 1324–1338. https://doi.org/10.1016/j.cell.2014.03.060.

32. Lv, J., Feng, Z.P., Chen, F.K., Liu, C., Jia, L., Liu, P.J., Yang, C.Z., Hou, F., and Deng, Z.Y. (2021). M2-like tumor-associated macrophages-secreted Wnt1 and Wnt3a promotes dedifferentiation and metastasis via activating beta-catenin pathway in thyroid cancer. Mol. Carcinog. 60, 25–37. https://doi.org/10.1002/mc.23268.

33. Wang, X., Yang, Y., and Huycke, M.M. (2017). Commensal-infected macrophages induce dedifferentiation and reprogramming of epithelial cells during colorectal carcinogenesis. Oncotarget 8, 102176–102190. https://doi.org/10.18632/oncotarget.22250.

34. Carlucci, F., Ishaque, A., Ling, G.S., Szajna, M., Sandison, A., Donatien, P., Cook, H.T., and Botto, M. (2016). C1q Modulates the Response to TLR7 Stimulation by Pristane-Primed Macrophages: Implications for Pristane-Induced Lupus. J. Immunol. 196, 1488–1494. https://doi.org/10.4049/jimmunol.1401009.

35. Sheng, J., Zhang, J., Wang, L., Tano, V., Tang, J., Wang, X., Wu, J., Song, J., Zhao, Y., Rong, J., et al. (2022). Topological analysis of hepatocellular carcinoma tumour microenvironment based on imaging mass cytometry reveals cellular neighbourhood regulated reversely by macrophages with different ontogeny. Gut 71, 1176–1191. https://doi.org/10.1136/gutjnl-2021-324339.

36. Szulzewsky, F., Pelz, A., Feng, X., Synowitz, M., Markovic, D., Langmann, T., Holtman, I.R., Wang, X., Eggen, B.J.L., Boddeke, H.W.G.M., et al. (2015). Glioma-associated microglia/macrophages display an expression profile different from M1 and M2 polarization and highly express Gpnmb and Spp1. PLoS One 10, e0116644. https://doi.org/10.1371/journal.pone.0116644.

37. Benlahrech, A., Duraisingham, S., King, D., Verhagen, L., Rozis, G., Amjadi, P., Ford, T., Kelleher, P., and Patterson, S. (2015). Human blood CD1c dendritic cells stimulate IL-12-independent IFN-gamma responses and have a strikingly low inflammatory profile. J. Leukoc. Biol. 97, 873–885. https://doi.org/10.1189/jlb.1A0114-058RR.

38. Guilliams, M., Bonnardel, J., Haest, B., Vanderborght, B., Wagner, C., Remmerie, A., Bujko, A., Martens, L., Thoné, T., Browaeys, R., et al. (2022). Spatial proteogenomics reveals distinct and evolutionarily conserved hepatic macrophage niches. Cell 185, 379–396.e38. https://doi.org/10.1016/j.cell.2021.12.018.

39. Browaeys, R., Saelens, W., and Saeys, Y. (2020). NicheNet: modeling intercellular communication by linking ligands to target genes. Nat. Methods 17, 159–162. https://doi.org/10.1038/s41592-019-0667-5.

40. Nakano, M., Kikushige, Y., Miyawaki, K., Kunisaki, Y., Mizuno, S., Takenaka, K., Tamura, S., Okumura, Y., Ito, M., Ariyama, H., et al. (2019). Dedifferentiation process driven by TGF-beta signaling enhances stem cell properties in human colorectal cancer. Oncogene 38, 780–793. https://doi.org/10.1038/s41388-018-0480-0.

41. Boudot, A., Kerdivel, G., Lecomte, S., Flouriot, G., Desille, M., Godey, F., Leveque, J., Tas, P., Le Dréan, Y., and Pakdel, F. (2014). COUP-TFI modifies CXCL12 and CXCR4 expression by activating EGF signaling and stimulates breast cancer cell migration. BMC Cancer 14, 407. https://doi.org/10.1186/1471-2407-14-407.

42. Li, L., Li, F., Xu, Z., Li, L., Hu, H., Li, Y., Yu, S., Wang, M., and Gao, L. (2023). Identification and validation of SERPINE1 as a prognostic and immunological biomarker in pan-cancer and in ccRCC. Front. Pharmacol. 14, 1213891. https://doi.org/10.3389/fphar.2023.1213891.

43. Yang, Y., and Cao, Y. (2022). The impact of VEGF on cancer metastasis and systemic disease. Semin. Cancer Biol. 86, 251–261. https://doi.org/10.1016/j.semcancer.2022.03.011.

44. Attisano, L., and Wrana, J.L. (2013). Signal integration in TGF-beta, WNT, and Hippo pathways. F1000prime Rep. 5, 17. https://doi.org/10.12703/P5-17.

45. Xu, S., Zhang, H., Chong, Y., Guan, B., and Guo, P. (2019). YAP Promotes VEGFA Expression and Tumor Angiogenesis Though Gli2 in Human Renal Cell Carcinoma. Arch. Med. Res. 50, 225–233. https://doi.org/10.1016/j.arcmed.2019.08.010.

46. Zhang, M., Yang, H., Wan, L., Wang, Z., Wang, H., Ge, C., Liu, Y., Hao, Y., Zhang, D., Shi, G., et al. (2020). Single-cell transcriptomic architecture and intercellular crosstalk of human intrahepatic cholangiocarcinoma. J. Hepatol. 73, 1118–1130. https://doi.org/10.1016/j.jhep.2020.05.039.

47. Tarique, A.A., Logan, J., Thomas, E., Holt, P.G., Sly, P.D., and Fantino, E. (2015). Phenotypic, functional, and plasticity features of classical and alternatively activated human macrophages. Am. J. Respir. Cell. Mol. Biol. 53, 676–688. https://doi.org/10.1165/rcmb.2015-0012OC.

48. Li, J., Diao, B., Guo, S., Huang, X., Yang, C., Feng, Z., Yan, W., Ning, Q., Zheng, L., Chen, Y., and Wu, Y. (2017). VSIG4 inhibits proinflammatory macrophage activation by reprogramming mitochondrial pyruvate metabolism. Nat. Commun. 8, 1322. https://doi.org/10.1038/s41467-017-01327-4.

49. Barkal, A.A., Weiskopf, K., Kao, K.S., Gordon, S.R., Rosental, B., Yiu, Y.Y., George, B.M., Markovic, M., Ring, N.G., Tsai, J.M., et al. (2018). Engagement of MHC class I by the inhibitory receptor LILRB1 suppresses macrophages and is a target of cancer immunotherapy. Nat. Immunol. 19, 76–84. https://doi.org/10.1038/s41590-017-0004-z.

50. Chen, H.M., van der Touw, W., Wang, Y.S., Kang, K., Mai, S., Zhang, J., Alsina-Beauchamp, D., Duty, J.A., Mungamuri, S.K., Zhang, B., et al. (2018). Blocking immunoinhibitory receptor LILRB2 reprograms tumor-associated myeloid cells and promotes antitumor immunity. J. Clin. Invest. 128, 5647–5662. https://doi.org/10.1172/JCI97570.

51. Saha, D., Martuza, R.L., and Rabkin, S.D. (2017). Macrophage Polarization Contributes to Glioblastoma Eradication by Combination Immunovirotherapy and Immune Checkpoint Blockade. Cancer Cell. 32, 253–267.e5. https://doi.org/10.1016/j.ccell.2017.07.006.

52. Morrissey, M.A., Kern, N., and Vale, R.D. (2020). CD47 Ligation Repositions the Inhibitory Receptor SIRPA to Suppress Integrin Activation and Phagocytosis. Immunity 53, 290–302.e6. https://doi.org/10.1016/j.immuni.2020.07.008.

53. Zeggar, S., Watanabe, K.S., Teshigawara, S., Hiramatsu, S., Katsuyama, T., Katsuyama, E., Watanabe, H., Matsumoto, Y., Kawabata, T., Sada, K.E., et al. (2018). Role of Lgals9 Deficiency in Attenuating Nephritis and Arthritis in BALB/c Mice in a Pristane-Induced Lupus Model. Arthritis Rheumatol. *70*, 1089–1101. https://doi.org/10.1002/art.40467.

54. Kang, X., Kim, J., Deng, M., John, S., Chen, H., Wu, G., Phan, H., and Zhang, C.C. (2016). Inhibitory leukocyte immunoglobulin-like receptors: Immune checkpoint proteins and tumor sustaining factors. Cell Cycle *15*, 25–40. https://doi.org/10.1080/15384101.2015.1121324.

55. Soncin, I., Sheng, J., Chen, Q., Foo, S., Duan, K., Lum, J., Poidinger, M., Zolezzi, F., Karjalainen, K., and Ruedl, C. (2018). The tumour microenvironment creates a niche for the self-renewal of tumour-promoting macrophages in colon adenoma. Nat. Commun. *9*, 582. https://doi.org/10.1038/s41467-018-02834-8.

56. Lai, S.M., Sheng, J., Gupta, P., Renia, L., Duan, K., Zolezzi, F., Karjalainen, K., Newell, E.W., and Ruedl, C. (2018). Organ-Specific Fate, Recruitment, and Refilling Dynamics of Tissue-Resident Macrophages during Blood-Stage Malaria. Cell Rep. *25*, 3099–3109.e3. https://doi.org/10.1016/j.celrep.2018.11.059.

57. Chen, X., and Calvisi, D.F. (2014). Hydrodynamic transfection for generation of novel mouse models for liver cancer research. Am. J. Pathol. *184*, 912–923. https://doi.org/10.1016/j.ajpath.2013.12.002.

58. Wang, G., Wang, Q., Liang, N., Xue, H., Yang, T., Chen, X., Qiu, Z., Zeng, C., Sun, T., Yuan, W., et al. (2020). Oncogenic driver genes and tumor microenvironment determine the type of liver cancer. Cell Death Dis. *11*, 313. https://doi.org/10.1038/s41419-020-2509-x.

59. Wang, S., Wang, R., Hu, D., Zhang, C., Cao, P., and Huang, J. (2024). Machine learning reveals diverse cell death patterns in lung adenocarcinoma prognosis and therapy. NPJ Precis. Oncol. *8*, 49. https://doi.org/10.1038/s41698-024-00538-5.

60. Tang, Q., Chen, J., Di, Z., Yuan, W., Zhou, Z., Liu, Z., Han, S., Liu, Y., Ying, G., Shu, X., and Di, M. (2020). TM4SF1 promotes EMT and cancer stemness via the Wnt/β-catenin/SOX2 pathway in colorectal cancer. J. Exp. Clin. Cancer Res. *39*, 232. https://doi.org/10.1186/s13046-020-01690-z.

61. Yang, S.B., Zhou, Z.H., Lei, J., Li, X.W., Chen, Q., Li, B., Zhang, Y.W., Ge, Y.Z., and Zuo, S. (2023). TM4SF1 upregulates MYH9 to activate the NOTCH pathway to promote cancer stemness and lenvatinib resistance in HCC. Biol. Direct *18*, 18. https://doi.org/10.1186/s13062-023-00376-8.

62. Hayakawa, Y., Tsuboi, M., Asfaha, S., Kinoshita, H., Niikura, R., Konishi, M., Hata, M., Oya, Y., Kim, W., Middelhoff, M., et al. (2019). BHLHA15-Positive Secretory Precursor Cells Can Give Rise to Tumors in Intestine and Colon in Mice. Gastroenterology *156*, 1066–1081.e16. https://doi.org/10.1053/j.gastro.2018.11.024.

63. Zhang, Y., Xu, H., Cui, G., Liang, B., Chen, X., Ko, S., Affo, S., Song, X., Liao, Y., Feng, J., et al. (2022). beta-Catenin sustains and is required for YES-associated protein oncogenic activity in cholangiocarcinoma. Gastroenterology *163*, 481–494. https://doi.org/10.1053/j.gastro.2022.04.028.

64. Neubert, E.N., DeRogatis, J.M., Lewis, S.A., Viramontes, K.M., Ortega, P., Henriquez, M.L., Buisson, R., Messaoudi, I., and Tinoco, R. (2023). HMGB2 regulates the differentiation and stemness of exhausted CD8(+) T cells during chronic viral infection and cancer. Nat. Commun. *14*, 5631. https://doi.org/10.1038/s41467-023-41352-0.

65. Wang, L., Guo, W., Guo, Z., Yu, J., Tan, J., Simons, D.L., Hu, K., Liu, X., Zhou, Q., Zheng, Y., et al. (2024). PD-L1-expressing tumor-associated macrophages are immunostimulatory and associate with good clinical outcome in human breast cancer. Cell Rep. Med. *5*, 101420. https://doi.org/10.1016/j.xcrm.2024.101420.

66. Kim, W., Chu, T.H., Nienhüser, H., Jiang, Z., Del Portillo, A., Remotti, H.E., White, R.A., Hayakawa, Y., Tomita, H., Fox, J.G., et al. (2021). PD-1 Signaling Promotes Tumor-Infiltrating Myeloid-Derived Suppressor Cells and Gastric Tumorigenesis in Mice. Gastroenterology *160*, 781–796. https://doi.org/10.1053/j.gastro.2020.10.036.

67. Qiu, X., Yang, S., Wang, S., Wu, J., Zheng, B., Wang, K., Shen, S., Jeong, S., Li, Z., Zhu, Y., et al. (2021). M(6)A Demethylase ALKBH5 Regulates PD-L1 Expression and Tumor Immunoenvironment in Intrahepatic Cholangiocarcinoma. Cancer Res. *81*, 4778–4793. https://doi.org/10.1158/0008-5472.Can-21-0468.

68. Li, C., Virgilio, M.C., Collins, K.L., and Welch, J.D. (2023). Multi-omic single-cell velocity models epigenome-transcriptome interactions and improves cell fate prediction. Nat. Biotechnol. *41*, 387–398. https://doi.org/10.1038/s41587-022-01476-y.

69. Bao, X., Li, Q., Chen, J., Chen, D., Ye, C., Dai, X., Wang, Y., Li, X., Rong, X., and Cheng, F. (2022). Molecular Subgroups of Intrahepatic Cholangiocarcinoma Discovered by Single-Cell RNA Sequencing-Assisted Multi-Omics Analysis. Cancer Immunol. Res. *10*, 811–828.

70. Bao, X., Li, Q., Chen, J., Chen, D., Ye, C., Dai, X., Wang, Y., Li, X., Rong, X., Cheng, F., et al. (2022). Molecular Subgroups of Intrahepatic Cholangiocarcinoma Discovered by Single-Cell RNA Sequencing-Assisted Multiomics Analysis. Cancer Immunol. Res. *10*, 811–828. https://doi.org/10.1158/2326-6066.Cir-21-1101.

71. Zhang, J., Song, J., Tang, S., Zhao, Y., Wang, L., Luo, Y., Tang, J., Ji, Y., Wang, X., Li, T., et al. (2023). Multi-omics analysis reveals the chemoresistance mechanism of proliferating tissue-resident macrophages in PDAC via metabolic adaptation. Cell Rep. *42*, 112620. https://doi.org/10.1016/j.celrep.2023.112620.

72. Guadayol, Ò., Thornton, K.L., and Humphries, S. (2017). Cell morphology governs directional control in swimming bacteria. Sci. Rep. *7*, 2061. https://doi.org/10.1038/s41598-017-01565-y.

73. Park, J.V., Chandra, R., Cai, L., Ganguly, D., Li, H., Toombs, J.E., Girard, L., Brekken, R.A., and Minna, J.D. (2022). Tumor Cells Modulate Macrophage Phenotype in a Novel In Vitro Co-Culture Model of the NSCLC Tumor Microenvironment. J. Thorac. Oncol. *17*, 1178–1191. https://doi.org/10.1016/j.jtho.2022.06.011.